

Review

Defect Engineering of Molybdenum-Based Materials for Electrocatalysis

Xiaoliang Gao ^{1,†}, Guolang Zhou ^{1,†}, Hao Wang ¹, Jingzhou Yin ^{1,*}, Lili Zhang ^{1,*}, Fei Xiao ², Kumar Siddharth ², Shangqian Zhu ² and Minhua Shao ^{2,3,4,5,*}

¹ Jiangsu Key Laboratory for Chemistry of Low-Dimensional Materials, Huaiyin Normal University, Huai'an 223001, China; gaoliangxl@163.com (X.G.); glzhou96@163.com (G.Z.); qingquWD@163.com (H.W.)

² Department of Chemical and Biological Engineering, The Hong Kong University of Science and Technology, Clear Water Bay, Kowloon, Hong Kong, China; fxiao@connect.ust.hk (F.X.); ksiddharth@connect.ust.hk (K.S.); kesqzhu@ust.hk (S.Z.)

³ Energy Institute, Chinese National Engineering Research Center for Control and Treatment of Heavy Metal Pollution, and Hong Kong Branch of the Southern Marine Science and Engineering Guangdong Laboratory The Hong Kong University of Science and Technology, Clear Water Bay, Kowloon, Hong Kong, China

⁴ Fok Ying Tung Research Institute, The Hong Kong University of Science and Technology, Guangzhou 511458, China

⁵ HKUST Shenzhen Research Institute, No. 9 Yuexing 1st RD, South Area, Hi-Tech Park, Nanshan, Shenzhen 518057, China

* Correspondence: jingzhouyin@hytc.edu.cn (J.Y.); zll@hytc.edu.cn (L.Z.); kemshao@ust.hk (M.S.)

† These authors contributed equally to this work.

Received: 30 September 2020; Accepted: 6 November 2020; Published: 10 November 2020



Abstract: Molybdenum-based electrocatalysts have been widely applied in electrochemical energy conversion reactions. The essential roles of defects, including doping, vacancies, grain boundaries, and dislocations in improving various electrocatalytic performances have been reported. This review describes the latest development of defect engineering in molybdenum-based materials for hydrogen evolution, oxygen reduction, oxygen evolution, and nitrogen reduction reactions. The types of defects, preparation methods, characterization techniques, and applications of molybdenum-based defect materials are elucidated. Finally, challenges and future research directions for these types of materials are also discussed.

Keywords: fuel cell; electrocatalysts; electrolyzer; water splitting; electrocatalysis

1. Introduction

In recent years, the increasing energy and environmental issues have prompted extensive research towards renewable, green, and sustainable energy saving, storage, and conversion systems [1,2]. Some of the prominent ones include water electrolytic technology [3], metal-air batteries [4,5], fuel cells [6], and ammonia synthesizing, involving crucial electrochemical reactions such as oxygen reduction/evolution, hydrogen oxidation/evolution, and the nitrogen reduction. However, one of the major obstacles to the practical applications is the rate of the electrochemical reactions involved [7]. Electrocatalysts play a key role in reducing the reaction kinetic barriers and promoting the efficiency and selectivity of the electrochemical reactions [8–10]. Hitherto, the most commonly used electrocatalysts are still noble metals, which hinder green technology commercialization due to high catalysts cost. Therefore, the exploration of highly efficient and cost-effective nonprecious metals with excellent performance is urgently needed [11,12]. Accordingly, electrocatalysts relying on inexpensive transition

metals, such as Ti, Cu, Mn, Ni, Co, and Mo have attracted much attention due to controllable architectures and excellent electrocatalytic applications among the noble metal alternatives [13].

Molybdenum (Mo)-based electrocatalysts are among candidates, having adjustable structure and good performances. Henceforth, Mo-based materials have been extensively studied, including Mo-based sulfides [14,15], phosphides [16,17], carbides [18,19], selenides [20], borides [21], nitrides [22], and oxides [23,24]. Interestingly, Mo-based materials have excellent electrocatalytic activity and stability in acidic [25], alkaline [26,27], and neutral [28] media. To date, researchers have developed several approaches towards synthesizing high-performance electrocatalysts, including optimizing morphology, pore size, three-dimensional framework to increase active sites, and compositing with carbon-based materials (graphene, CNT (carbon nanotube), etc.) to enhance conductivity [29–34]. Recent insights have illustrated that defect engineering is a valuable strategy to regulate the surface properties and electronic structure of catalysts and has been extensively used in electrode materials [35]. With the introduction of defect structures, the electron structure of the catalyst site is efficiently modified to promote the formation and transformation of intermediate states, thus accelerating the electrochemical process. However, because of the absence of high sophisticated characterization methods in the past, the effect of defects on the catalytic activity has not been thoroughly elucidated. Of late, numerous high-end apparatuses increasingly began to be employed in the research of defects, such as electron energy loss spectroscopy (EELS), and X-ray photoelectron spectroscopy (XPS), which can reveal information of defects such as the crystal structure, chemical bond, electronic structure, and surface shape, being useful in better comprehension of reaction mechanism. Furthermore, understanding the correlation between defects and catalytic performance in Mo-based materials is of great importance for the design of advanced electrocatalysts.

In this review, the role of defect engineering in Mo-based electrocatalysts is systematically introduced. Types of defects, preparation methods, characterization techniques, and their applications in hydrogen evolution reaction (HER), oxygen evolution reaction (OER), oxygen reduction reaction (ORR), and nitrogen reduction reaction (NRR) are also discussed in detail. Finally, challenges and future research directions of Mo-based materials for further applications are also discussed.

2. Defect Theory of Mo-Based Materials

2.1. Types of Defects

According to the dimensions, defects in catalysts can be grouped into four categories: 0-dimensional (0D) defects (e.g., vacancy and doping); 1-dimensional (1D) defects (e.g., edge dislocation and screw dislocation); 2-dimensional (2D) defects (e.g., grain boundary and twin boundary); and 3-dimensional (3D) defects (e.g., spatial lattice disorder) [36,37]. For Mo-based materials, according to the composition of the defect, 0D defects can be further classified into vacancies (including anion and cation vacancies) and doping (metal and non-metal atom doping). At present, the research on high-dimensional complex defects (including 1D, 2D, and 3D) in Mo-based materials is still at an early stage due to complexity of the structure. Therefore, the defect types can be divided into three categories: Vacancies, doping, and complex defects. In this part, we focus the applications of Mo-based material defect engineering in electrocatalysis according to these classifications.

2.1.1. Heteroatomic Doping

Heteroatomic doping is observed when different atoms enter the original lattice, which can be further classified into two categories according to chemical elements: Non-metal and metal heteroatomic doping.

Non-Metal Heteroatomic Doping

Typical non-metal heteroatomic doping of Mo-based materials includes nitrogen (N), oxygen (O), and carbon (C) atoms which can lead to changes in surface charge distribution and enhanced

electrocatalytic performance [28,38,39]. In one study, Chen et al. [40] prepared MoP with N-doping under plasma treatment, which enriched Mo-P active sites and leading to electron locating near doped sites (Figure 1a). This process not only improved surface activity, but also provided new chances to understand the electrocatalytic mechanism. In another study, Tang et al. [41] reported that the N doping can modulate the electronic properties of the active sites, cause lower free energy of adsorption and desorption for the hydrogen species involved in the reaction.

Metal Heteroatomic Doping

In addition to non-metal heteroatom-modified Mo-based materials, metal-heteroatom modified catalysts have also been widely studied. Researchers have demonstrated that metal atom doping could alter the electron distribution of adjacent atoms as well as regulating the interior catalytic activity of active sites, which caused improving electrocatalytic performance. For instance, Li and co-workers found that 2D molybdenum disulfide (MoS_2) doped with trace amount of Pd can increase the hydrogen adsorption energy [42] (Figure 1b). Other than Pd, other metal heteroatom doping could have a significant effect on electrocatalysts. For example, Zeng et al. [7] designed a kind of Ni-doped MoO_2 . In this study, density functional theory (DFT) calculations proved that Ni doping caused the lack of electrons around O atoms, and these electron-deficient sites increased the coverage of hydrogen on the catalyst surface.

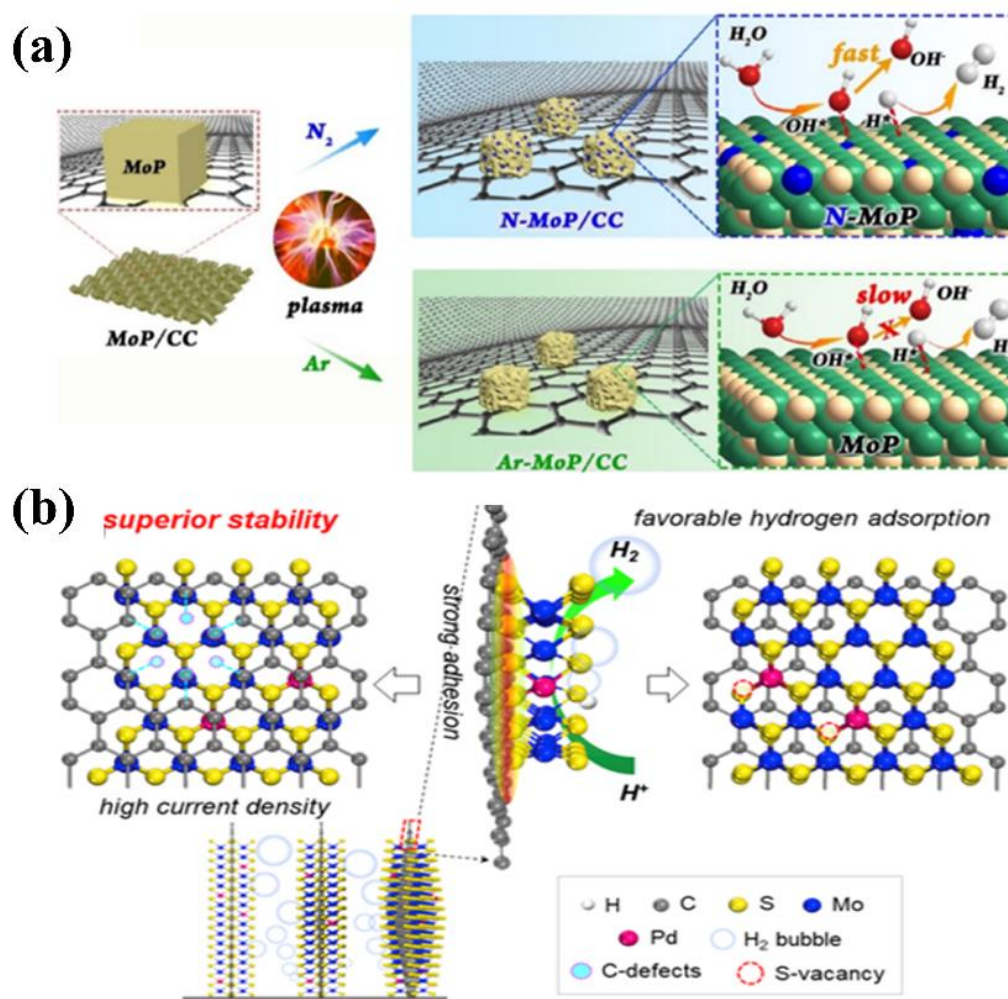


Figure 1. (a) schematic illustration for fabricating N-MoP/CC. Copyright 2020 Elsevier. (b) schematic illustration of hydrogen evolution catalyzed by palladium-doped MoS_2 anchored on vertical grapheme. Copyright 2020 Elsevier.

2.1.2. Vacancy Defects

Vacancies can regulate the active sites, electronic structure, and adsorption energies of catalysts [43]. Various vacancies such as O, S, P, and B have been reported to improve the performance of Mo-based catalysts recently [21,39,40,44,45]. Vacancy defects from Mo-based catalysts, especially O ones, are easy to obtain. For example, Tong et al. [43] designed NiMoO₄ nanosheets with oxygen vacancy-rich as a sample to establish the connection with O vacancies and urea oxidation reaction (UOR) activity. Experimental and theoretical results confirmed that the O vacancies could generate synergetic effects of faster electron transport, more exposed active sites, and lower adsorption energy of urea molecules. Besides O vacancies, other atomic vacancies in Mo-based catalysts have also been constructed. In particular, metal vacancies can increase the valence state of the metal centers around the vacancies because of the diversity of electron and orbital distribution. As shown in the Figure 2a, Li et al. [31] investigated Mo_xC with contained Mo vacancies and macro-porous opal-like (IOL) structure and found that the Mo vacancies modulated the hydrogen binding energy, stabilized IOL structure, and accelerated mass/charge transport, resulting in enhanced HER performance.

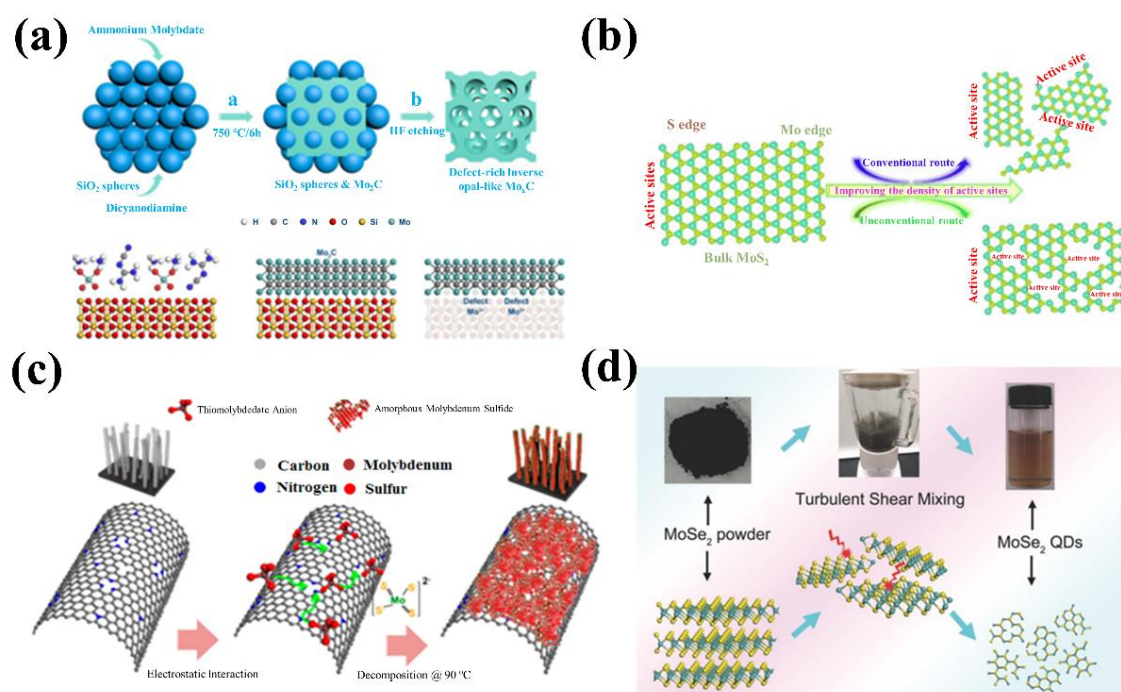


Figure 2. (a) schematic illustration for synthesis of inverse opal-like Mo₂C with SiO₂ spheres and the formation of a rich density of defects. Copyright 2017 American Chemical Society. (b) schematic illustration of the formation of active sites in MoS₂. Copyright 2014 Wiley. (c) schematic illustration of three-dimensional hybrid catalyst synthesis. Copyright 2014 American Chemical Society. (d) schematic diagram of the TSM (turbulent shear mixing) process for preparing MoSe₂ QDs from bulk MoSe₂. Copyright 2017 Wiley.

2.1.3. Complex Defects

In addition to the above types of point defects, other types, such as carrier defects and high-dimensional complex defects also possess great significance in improving electrocatalytic performances. For instance, Li et al. [46] discovered that electron-rich N species in amorphous molybdenum sulfide (MoS_x) layer directly bound at N-doped carbon nanotube provided extra electrons to graphitic carbons, resulting in high electro conductivity for HER (Figure 2c). Furthermore, highly electronegative N species can greatly ameliorate surface energy and provide favorable reaction affinity for MoS_x without any intermediate adhesive layer. Except for defects on the carrier, other

defects on Mo-based materials could also be engineered such as lattice defects or edge dislocation. Recently, Qu et al. [20] developed a novel top-down approach to maximize catalytic edge sites of MoSe₂ by breaking up bulk MoSe₂ into quantum dots (QDs) (Figure 2d). These MoSe₂ QDs provided a high fraction of atoms in reactive edge sites, thus improving the catalytic activities. Moreover, Zhang et al. [47] obtained the 3D defect-rich MoS₂ mesh/rGO (reduced graphene oxide) foam through the simple anion replacement in hydrothermal reaction (Figure 2b).

3. Defect-Inducing Strategies

A large number of theoretical and experimental studies have established that the presence of defects in Mo-based materials affects the electrocatalytic performance. Over the years, several strategies for the preparation of miscellaneous Mo-based defect materials have been developed. The choice of preparation method usually depends on the bulk structure of the catalyst and the type of defects required. Therefore, it is required to discuss synthesis strategies from the perspective of defect types to construct specific types of defects and deepen the understanding of defect formation process.

3.1. Generation of Heteroatomic Doping Defects

Recently, a series of studies have reported the successful preparation of electrocatalysts with heteroatoms doping. Among them, solvothermal/hydrothermal and high-temperature pyrolysis are two commonly used methods for preparing doped defects. The hydrothermal and solvothermal methods are high-temperature and high-pressure reactions carried out in a closed container with water or organic solvents as the medium. The product is gradually formed as the temperature increases, which provides the driving force for the dispersed reactants. Therefore, if the heteroatom precursor is added to the raw material, it can easily enter the crystal lattice of the product to form doping defects. For example, Liu et al. designed oxygen-incorporated MoS₂ nanosheets decorated on reduced graphene oxide (O-MoS₂/rGO) via a solvent-assisted hydrothermal method (Figure 3a) [48]. The enhanced HER performance of this catalyst was due to the improved intrinsic conductivity from oxygen incorporation and the obvious synergetic effect between MoS₂ nanosheets and rGO.

Additionally, the doping defects introduced by high-temperature pyrolysis are usually the doping of non-metal atoms (such as N, P, C, and S). For example, Yang et al. synthesized ultrafine β-Mo₂C nanoparticles confined within hollow capsules of N-doped porous carbon (β-Mo₂C@NPCC) via pyrolysis of ZIF-8 nanocrystals covered with a Mo-tannic acid coordination polymer, as shown in the Figure 3b [49]. The surface Mo atoms of β-Mo₂C were then oxidized in-situ into an ultrathin Mo–O layer by exposure to air at room temperature. In another study, Xiao's group found that CoMoP in lower valence states enhanced the stability and catalytic activity which resulted in raising of the d-band center of Mo in CoMoP and the phosphorization process improving the adhesion of the CoMo-based cuboids on the Ni substrate (Figure 3c) [50].

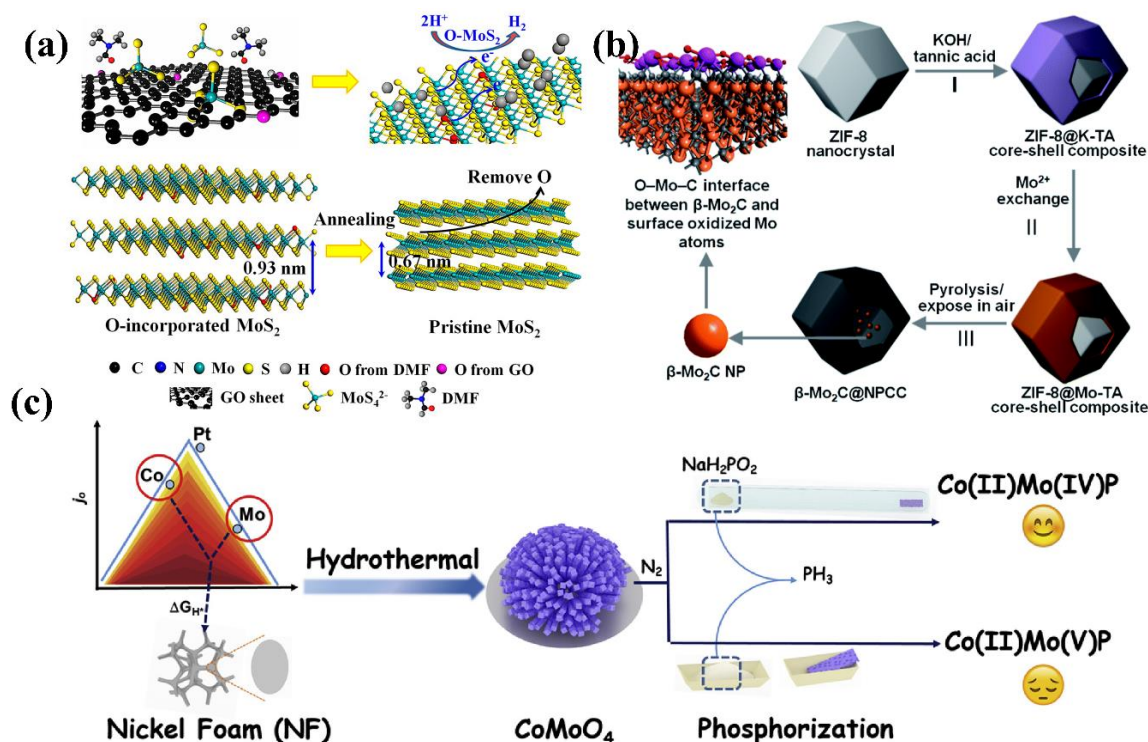


Figure 3. (a) growth scheme of vertically aligned oxygen-incorporated MoS₂ nanosheets decorated on reduced graphene oxide (O-MoS₂/rGO) catalysts. Copyright 2016 American Chemical Society. (b) synthetic scheme for the preparation of β-Mo₂C nanoparticles confined within hollow capsules of N-doped porous carbon (β-Mo₂C@NPCC). Copyright 2020 Royal Society of Chemistry. (c) schematic illustration of the synthesis of CoMoP catalysts. Copyright 2019 Elsevier.

3.2. Method of Preparing Vacancy Defects

In addition to solvothermal/hydrothermal and pyrolysis, other methods for preparing vacancy defects are mainly external force induction methods and chemical etching. Laser ablation in liquid (LAL) is a controllable, green, and fast technology that has been widely used in the synthesis of nanomaterials [51]. Laser ablation instantly generates very high pressure and temperature. Through rapid quenching within the interval of laser pulses, the constituent atoms of the Mo-based material may break free from the bondage of chemical bonds and form vacancy defects (such as O, S, and N vacancies). As illustrated in Figure 4a, Zhou's group created S-vacancies in the basal plane of MoS₂ nanosheets by using LAL [52].

Similar to the LAL method, other external force induction methods such as plasma-assisted method [53], ball milling [54], spray drying [55], turbo shear method [56], and microwave treatment [57] can also lead to various vacancy defects. For example, Lu et al. designed S vacancies and strain in amorphous Mo sulfide through hydrogen plasma (Figure 4b) [58]. In another study, Panda and coworkers developed MoS₂-rGO with S vacancies via an aqueous-solution-based spray drying route (Figure 4c) [55]. These methods are also feasible in creation of other vacancies. For instance, Datta et al. fabricated oxygen deficient 2D α-MoO_{3-x} nanosheets via a liquid phase exfoliation method (Figure 4d) [23]. In the chemical etching process, strong acids, strong bases, and strong oxidants or reducing agents are used to treat Mo-based materials [59]. In harsh chemical environments, Mo-based materials usually form abundant defects [9]. In one such investigation, Wang et al. prepared a large number of uniformly distributed S vacancies on the surface of MoS₂ by using hydrogen peroxide as an etchant [59].

3.3. Strategies of Complex Defects Design

It is very difficult to prepare single type of high-dimensional complex defects such as grain boundaries, dislocations, and bulk defects. Generally, multiple types of defects will emerge simultaneously in the process of developing high-dimensional complex defects. There are two methods for designing complex defects; the bottom-up method and the top-down method. The bottom-up method creates defects during the synthesis of Mo-based materials. Several strategies such as solvothermal/hydrothermal synthesis [60,61], one-pot microwave [57], and ball-milling [62] have been adopted over the years. For example, Sarker et al. synthesized MoSe_2/rGO with multiple complex defects in one step using Se precursor and rGO as raw materials under microwave-assisted conditions [57].

The top-down synthesis method is utilized to obtain the defect structure through post-processing after the sample is synthesized. Unlike the bottom-up method, the formation of defects and sample preparation in this method is not performed at the same time. In one study, Zhang et al. proposed a method of post-processing using an arc to obtain MoS_2 with complex defects [63]. In the process of arc smelting, the composition of MoS_2 did not change, but a lot of defects could be formed on the surface. Other synthesis methods such as laser ablation, plasma radiation, ball milling, turbulent shear, vapor phase stripping, and etching methods can also be applied on samples to obtain various such defect structures [53,64].

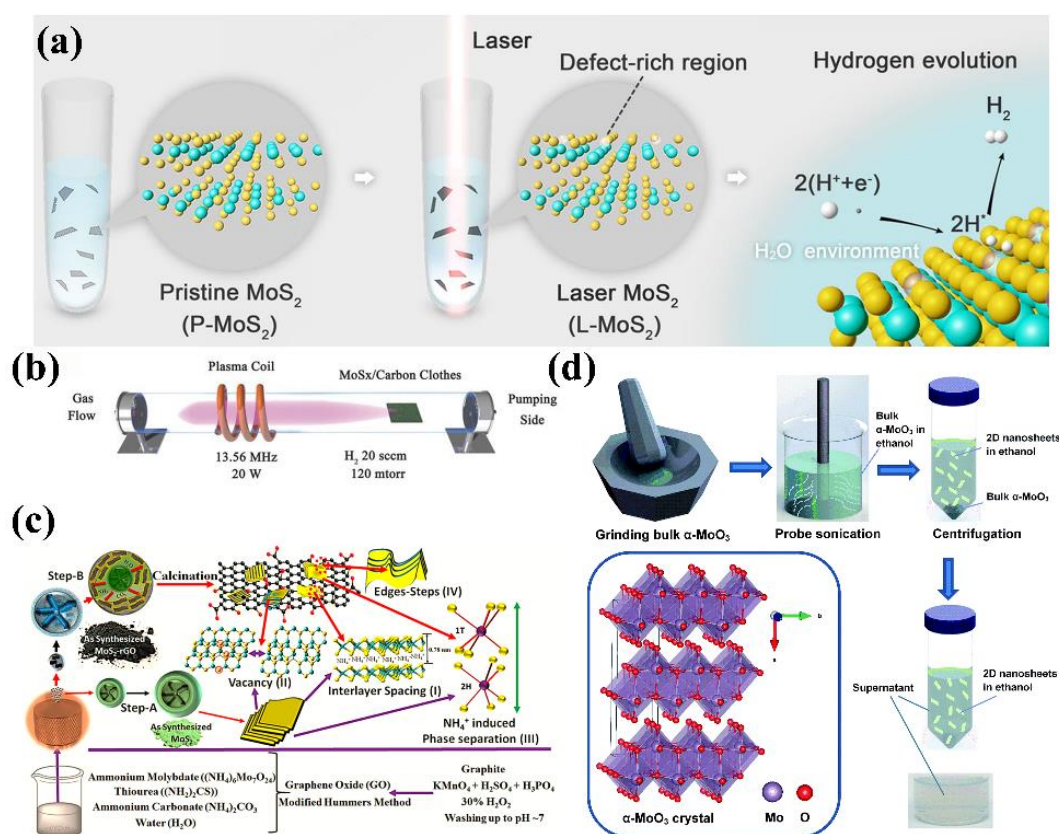


Figure 4. (a) synthetic procedure of L-MoS₂. Color code: Cyan represents Mo, yellow represents S, white represents H, and transparent color represents vacancy. Copyright 2019 American Chemical Society. (b) schematic illustration for the experimental setup of inductively coupled plasma. Copyright 2016 Wiley. (c) schematic representation of developed synthetic strategy for bare MoS₂ and MoS₂-rGO nanocomposite sheets and corresponding defects. Copyright 2018 American Chemical Society. (d) a schematic diagram describing the step-by-step synthesis process from bulk α -MoO₃ to 2D nanosheets. Copyright 2017 Royal Society of Chemistry.

4. Advanced Characterization Techniques for Defect Structure Analysis

Some advanced characterization techniques can directly observe or indirectly prove the presence of various defects, which could provide useful guidelines for the rational design of defect structure as well as better understanding of structure-activity relationships.

4.1. Microscopy Characterization

Microscopic observation can help researchers distinguish various defects in the lattice of Mo-based catalytic materials, this is beneficial for targeted design of desired defect structures. Usually, complex defects can be observed via electron microscope clearly due to larger size. Other defects (such as doping and vacancies) are difficult to be observed by the traditional electron microscope. Therefore, microscopic techniques are generally used to analyze complex defects, and point defects are usually characterized by spectroscopy.

Transmission electron microscopy (TEM) and high-resolution transmission electron microscopy (HRTEM) not only can observe the surface defects directly but also the internal defects clearly. For example, as shown in Figure 5a, the TEM image shows that the MoS₂ nanoflower possessed an ultra-thin lamellar structure with obvious curling and overlapping structures at the edges, while the HRTEM image illustrated the lattice fringes of the MoS₂ nanoflowers, which could provide the interlayer spacing of MoS₂ [56,65]. As shown in the Figure 5b, compared to the bulk MoSe₂, the interlayers of the MoSe₂ nanosheets were slightly expanded [20]. In an interesting study, Zhu et al. prepared MoSe₂ quantum dots using turbulent shear mixing technology and found that the areas marked with red and blue arrows in HRTEM (Figure 5c) show discontinuous lattice fringes, indicating defects in the MoSe₂ crystal [56]. Mo-based material with a single defect structure is difficult to obtain due to the limitation of synthesis technology. At present, the defect engineering of Mo-based materials with multiple defects reported in the literature can also be characterized via HRTEM. For example, Lin et al. found that the lattice stripes (marked in circle) were obviously broken in the HRTEM image of MoS₂/NiS₂ heterojunction (Figure 5d) [60]. Moreover, the hetero-interface between the MoS₂ crystal and the NiS₂ crystal could be observed in the place indicated by the red arrow above, which proved the multiple composite defects at the same time. Scanning transmission electron microscope (STEM) is a microscopic characterization with ultra-high resolution. Ou et al. characterized the molybdenum sulfide quantum dots by using a high-angle annular dark field scanning transmission electron microscope (HAADF-STEM), in which a variety of defects such as atomic vacancies, lattice distortion, and lattice fragmentation at the edges could be observed (Figure 5e) [51]. Similarly, STEM and energy dispersive spectroscopy (EDS) or STEM and EELS are usually used in combination to further analyze the elemental distribution and single-atom defects in the material [66]. For example, Kwon et al. used EELS to identify Co atoms exclusively in the MoS₂ nanosheets and only Ru atoms in the Ru nanoparticles (Figure 5i). The data confirmed that the concentration of Ru in the MoS₂ nanosheets is almost zero and no Co doping occurs in the Ru nanoparticles [67]. Moreover, Figure 5j shows HAADF-STEM image and energy-dispersive X-ray spectroscopy (EDX) elemental mapping, and the corresponding EDX spectra which demonstrate the homogeneous distribution of Co, Mo, and S elements on the entire CoRu–MoS₂ sample [67].

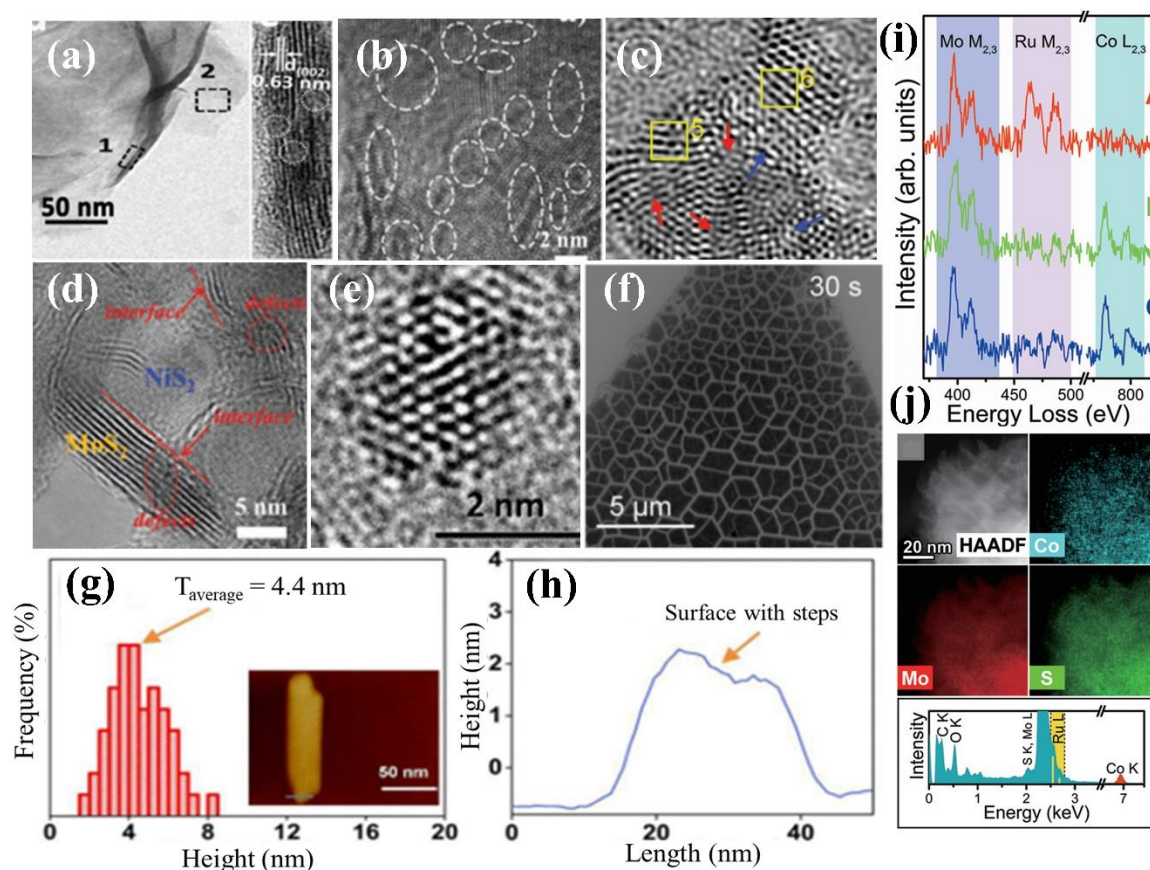


Figure 5. (a) TEM image for defect-rich MoS₂ nanoflower. Copyright 2018 Wiley. (b) high-resolution transmission electron microscopy (HRTEM) image of ultrathin MoSe₂ nanosheets. Copyright 2015 American Chemical Society. (c) HRTEM image of MoSe₂ quantum dots. Copyright 2017 Wiley. (d) HRTEM images of MoS₂/NiS₂ nanosheets. (e) high-angle annular dark field scanning transmission electron microscope (HAADF-STEM) image of molybdenum sulfide quantum dots. Copyright 2017 Springer. (f) SEM image of monolayer MoS₂ treated by plasma. Copyright 2016 American Chemical Society. (g) AFM figure of 2D a-MoO_{3-x} nanosheets, (g) frequency histogram of the observed thickness of the 2D nanosheets, atomic force microscope (AFM image of the nanosheet (inset), and (h) corresponding thickness profile. Copyright 2017 Royal Society of Chemistry. (i) background-subtracted Atomic-resolution electron energy loss spectrum (EELS) around the Mo_{2,3}-, Ru M_{2,3}-, and Co L_{2,3}-ionization edges. (j) HAADF-STEM images, energy-dispersive X-ray spectroscopy (EDX) elemental mapping of Co (K shell), Mo (L shell), and S (K shell), and their corresponding EDX spectra ([Co] = 10% and average [Ru] = 20%). Copyright 2020 Wiley.

Scanning electron microscope (SEM) is one of the most commonly used microscopic characterization techniques. Some larger defect structures can be directly observed with SEM. Ye et al. used SEM to observe the single-layer MoS₂ after plasma treatment. Clear cracks could be observed in Figure 5f, which indicated that a large number of cracks appear on the substrate of MoS₂ by plasma treatment [53]. In addition, EDS can also be combined with SEM to analyze the composition and distribution of the doping defects [18,21,68,69] when foreign atoms or ions are doped. Atomic force microscope (AFM) could be used to characterize the surface smoothness of the 2D materials. In one investigation, Datta et al. used AFM to study the surface of MoO₃ after liquid phase stripping. As shown in Figure 5g,h, the stripped 2D nanoflakes had a stepped base surface, which highlighted the existence of pits on the surface of MoO₃, resulting in more dangling bonds [23].

4.2. Crystallography Characterization

Powder X-ray diffraction (XRD) quickly analyzes the crystal phase structure of crystalline materials and can provide information about the size of crystal cells. Peaks in the XRD spectrum can shift or widen, and the corresponding unit cell parameters also changes when defects are introduced. Figure 6a represents XRD pattern of defective MoS₂ nanosheets, which highlighted that the defect-rich structure led to the formation of nanometer-sized domains along the basal planes, resulting in the broadening of the (100) and (110) diffraction peaks in the spectrum [70]. In one study, Tang et al. confirmed that interlayer expanded MoS₂ could be prepared via N-doped graphene oxide intercalation [71]. The peak at 14.2° was the (002) plane, corresponding to a layer spacing of 6.2 Å for MoS₂ (Figure 6b). When the reaction temperature decreases, two new diffraction peaks could be observed at 9.3° and 18.6°, corresponding to the interlayer spacing of MoS₂ of 9.5 and 4.7 Å, respectively. These results indicated that the interlayer of MoS₂ can expand with the intercalation of N-doped graphene oxide at a relative low temperature [71]. In an interesting study (Figure 6c,d), XRD patterns and corresponding cell parameters of Mo₂C doped with different amounts of Co was elucidated. It was observed that all peaks in XRD pattern shifted, and as the amount of Co doping increased, the degree of shift also increased. The corresponding unit cell parameters (a, b, and c) and unit cell volume decreased with the increase of Co doping, indicating that Co doping can cause shrinking of Mo₂C unit cell [72].

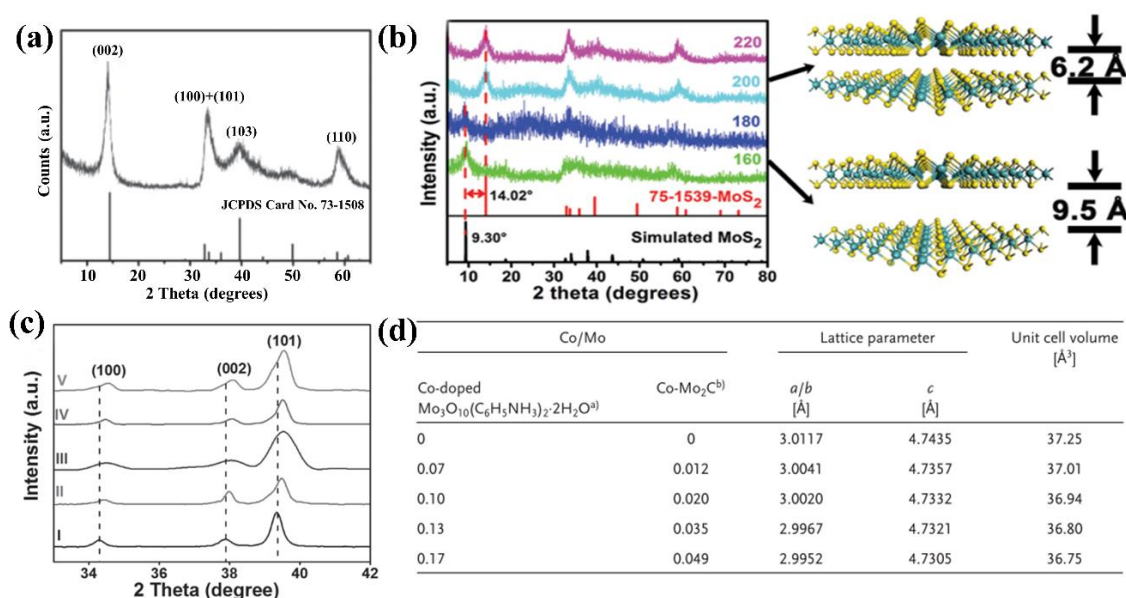


Figure 6. (a) XRD pattern of defect-rich MoS₂ ultrathin nanosheets. Copyright 2013 Wiley. (b) XRD patterns of MoS₂/N-RGO-T nanocomposite prepared at different temperatures from 160 to 220 °C, at the right, structural models of MoS₂ with the interlayer spacing of 6.2 and 9.5 Å, respectively. Copyright 2016 Wiley. (c) XRD patterns of (I) Mo₂C, (II) Co-Mo₂C-0.012, (III) Co-Mo₂C-0.020, (IV) Co-Mo₂C-0.035, and (V) Co-Mo₂C-0.049. (d) value of lattice parameters and unit cell volume for Mo₂C in Co-Mo₂C with distinct Co/Mo ratio. Copyright 2016 Wiley.

4.3. Spectroscopy Characterization

While microscopic characterization can provide atomic-scale images of defect structures, it suffers from issues like complex sample preparation processes and small characterization regions. Therefore, these techniques cannot offer information on the electronic structure, lattice vibrations, and so on. Spectroscopic methods such as Raman spectroscopy and photoluminescence spectroscopy (PL) are nondestructive testing methods and can offer abundant information about the crystal structure, electronic structure, defect density, and lattice vibrations, thus show a significant role in the characterization of defects in Mo-based materials.

Raman spectroscopy is widely used to determine the type and number of defects in Mo-based materials, and to characterize defects and electron band structures [47,73]. As shown in Figure 7a, the two peaks of A-MoS_x (treated with arc-melting) A_{1g} and E_{2g}¹ of A-MoS_x were wider than those of MoS₂, and these peaks shifted after arc smelting [63]. The results portrayed that arc smelting produces a disordered structure in MoS₂. In another investigation (Figure 7b), the Raman spectrum of MoS₂ QDs and bulk MoS₂ were illustrated. The Raman spectra of MoS₂ QDs illustrated a damping of the disorder-activated side bands together with the blue shift of E_{2g} and red shift of the A_{1g} peaks, which were consistent with the increase of edge S vacancies. The decreased intensities of the A_{1g} and E_{2g} peaks highlighted the decrease in size of the MoS₂ nanosheets [74]. Due to the poor conductivity of Mo-based materials, researchers usually use carbon materials as support to enhance the electrocatalytic performance [38,75–77]. Raman spectroscopy has a unique application in characterizing defects in carbon materials. For example, D-peak (at about 1360 cm⁻¹) in Figure 7c pinpointed the presence of a defective structure [57]. In most cases, researchers use I_D/I_G (Intensity of D peak/Intensity of G peak) ratio to reflect the degree of defects in the carbon material, with this value increasing as the concentration of defects increases [78].

Unpaired electrons caused by unsaturated coordination structures (e.g., vacancies) in Mo-based materials are commonly measured using electron paramagnetic resonance (ESR or EPR) [61,68]. It was observed that bulk MoS₂ did not produce an EPR signal (Figure 7d). Ionizing radiation caused MoS₂ to generate S vacancies and then EPR signal was observed, with the signal gradually increasing as the radiation time increased [64]. Interestingly, very strong bound exciting emission peaks will appear in the low-temperature photoluminescence spectrum (PL), when point defects exist in Mo-based materials [30,39]. Figure 7e shows the PL spectra of the bilayer MoS₂ treated with UV-ozone. Proper UV exposure can increase the O content in MoS₂, which increased the intensity of the peak in PL spectrum and caused the red-shift. The red shift is attributed to these O defects, which change or cause extra radioactive recombination of the electrons at shallow defect states and holes in the valence band [79].

Positron annihilation spectroscopy (PAS) provides direct information about defect structure, such as concentration and type, by detecting the lifetime of positrons [58,80]. The positron lifetime spectrum such as in Figure 7f could be fitted to an exponential function corresponding to three components at different annihilation locations which indicate the characteristics of defects [65]. Due to the speedy progress of synchrotron radiation sources, X-ray absorption spectroscopy (XAS) has become a widespread characterization method. Owing to the different energy relative absorption thresholds, XAS can be divided into two parts; X-ray absorption near edge structure (XANES) and extended X-ray absorption fine structure (EXAFS) [81]. These measurements can offer a great deal of information about the structure of the defective catalyst, such as structural symmetry, chemical state (elemental valence), and bonding of the atoms. For instance, Yang et al. used XAS to study the doping of metal atoms in MoS₂ as shown in Figure 7g,h. The Pd K-edge XANES spectra revealed that Co-Pd-MoS₂ possessed higher energy compared with pure Pd foil (Figure 7g). The Fourier transform of the k³-weighted Pd K-edge EXAFS spectra for Co-Pd-MoS₂ (Figure 7h) portrayed a lower R position than that in Pd foil, demonstrating Pd atoms occupying the sites of Mo atoms instead of forming Pd particles [82]. In another study (Figure 7i), the pre-edge feature of the sulfur L-edge was elucidated. Due to the highly covalent molecular orbital, MoS₂@SWNT exhibited a broadened peak in this region and shifted slightly towards the high energy direction, indicating that S existed in an unsaturated form with apical S²⁻ or bridging disulfide S₂²⁻ coordination [83].

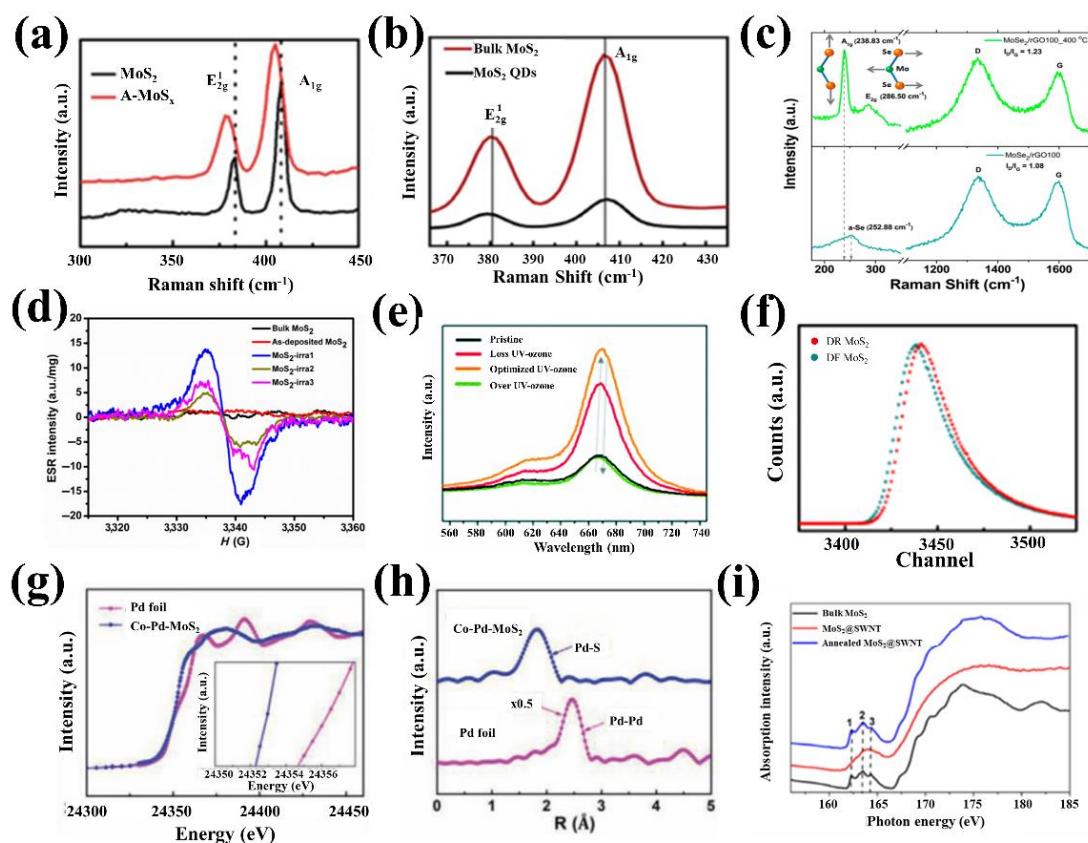


Figure 7. (a) raman spectra of A-MoS_x and MoS₂. Copyright 2016 Royal Society of Chemistry. (b) raman spectrum of bulk MoS₂ and MoS₂ QDs. Copyright 2019 Elsevier. (c) raman spectra of MoSe₂/rGO100 and MoSe₂/rGO100_400 °C with illustration of atomic vibration of A_{1g} (left) and E_{2g}¹ (right) as inserted. Copyright 2018 American Chemical Society. (d) ESR spectra of MoS₂. Copyright 2019 Springer. (e) PL spectra of the bilayer MoS₂ with increasing UV–ozone treatment. Copyright 2019 Royal Society of Chemistry. (f) positron annihilation lifetime spectroscopy of two samples and fitting results. Copyright 2018 Wiley. (g) the normalized Pd K-edge X-ray absorption near edge structure (XANES) spectra. Inset: The enlarged Pd K-edge XANES spectra. (h) Fourier transforms of k₃-weighted Pd K-edge of the extended X-ray absorption fine structure (EXAFS) spectra of Co-Pd-MoS₂ and Pd foil, demonstrating Pd has replaced Mo atoms successfully instead of forming particles or clusters. Copyright 2020 Wiley. (i) S L-edge XANES spectra of bulk MoS₂, MoS₂@SWNT hybrid, and the annealed hybrid, indicating transitions of S_{2p} electrons to unoccupied s- or d-like states. Copyright 2016 Springer.

5. Applications of Mo-Based Materials in Electrochemical Energy Conversion

5.1. Hydrogen Evolution Reaction

HER has been considered as one of sustainable solutions for enhancing production of hydrogen and reducing the release of greenhouse gases from water splitting. There has been a lot of efforts to explore non-precious metal electrocatalysts with high activity, durability, and high stability for HER, which proceeds via Heyrovsky and Tafel steps or Volmer [84]. In the first Volmer step, the hydrated proton is reduced at the catalytic site (M) to form an intermediate state that adsorbs hydrogen atoms: $H^+ + M + e^- = MH_{ads}$. The second step of the reaction depends on the coverage of H_{ads} on the catalyst surface. When the coverage of H_{ads} is relatively low, a Heyrovsky reaction occurs, i.e., the adsorbed hydrogen atoms combines with the electrons and protons in the electrolyte to form hydrogen: $MH_{ads} + H^+ + e^- = M + H_2$, where this reaction is also called the electrochemical desorption step. While with the high coverage of H_{ads} , a recombination reaction occurs between adjacent adsorbed hydrogen atoms, and this process is also called the chemical desorption step: $2MH_{ads} = 2M + H_2$ (Tafel reaction). Under alkaline and neutral

conditions, due to the lack of abundant protons, the Volmer reaction is slower because it involves the dissociation of water before hydrogen adsorption. The reaction mechanism involved is the following equations: $\text{H}_2\text{O} + \text{M} + \text{e}^- = \text{MH}_{\text{ads}} + \text{OH}^-$; $\text{MH}_{\text{ads}} + \text{H}_2\text{O} + \text{e}^- = \text{M} + \text{OH}^- + \text{H}_2$; and $2\text{MH}_{\text{ads}} = 2\text{M} + \text{H}_2$. Both adsorption (Volmer reaction) and desorption (Heyrovsky or Tafel reaction) steps may become rate limiting processes [85]. Therefore, the adsorption energy of hydrogen (H_{ads}) is a key factor affecting the electrocatalytic performance [86].

In a significant study, Jaramillo et al. plotted the volcano graph of exchange current density with adsorption Gibbs free energy (Figure 8) [86]. Theoretically, the catalyst located at the top of this volcano curve has the best HER activity. It can be observed from Figure 8 that the precious metal Pt has the best electrocatalytic activity. On the contrary, metallic Mo and MoS_2 possess limited catalytic activity. Introduction of other metal or non-metallic elements to form alloys or compounds with doping or vacancy defects, or the introduction of complex defects can effectively adjust the electronic structure and endow Mo-based materials with more energy suitable for hydrogen adsorption [87].

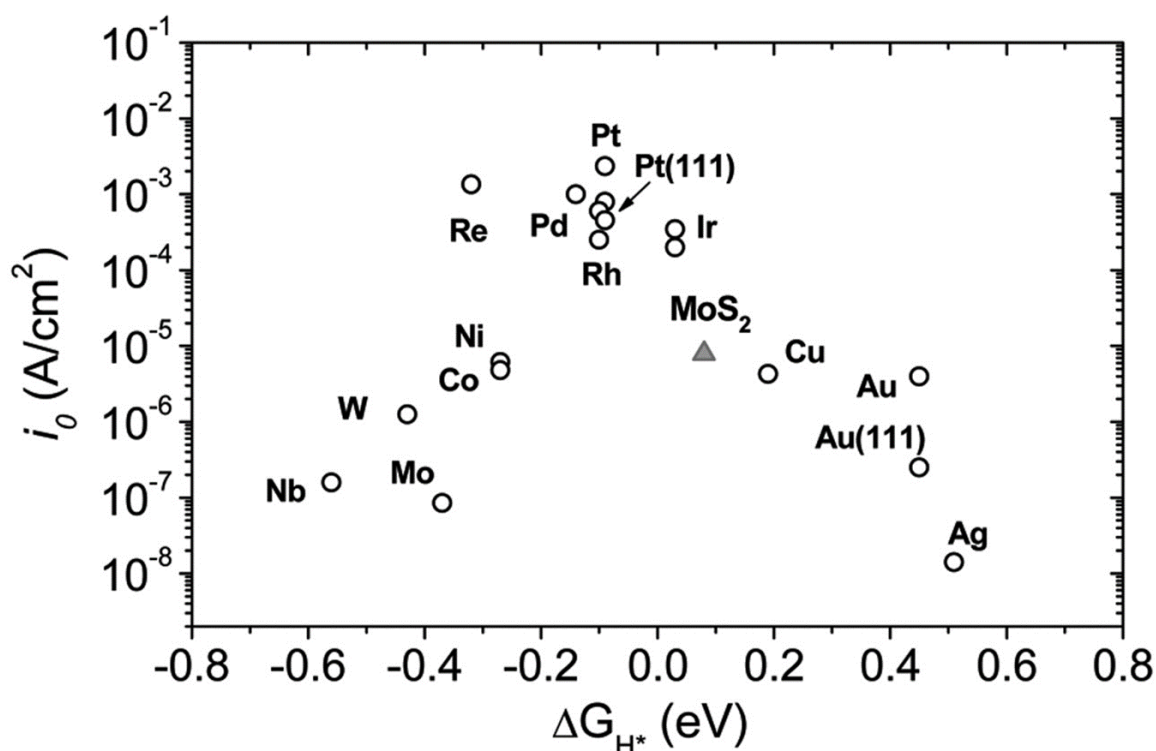


Figure 8. Volcano plot of the exchange current density as a function of the density functional theory (DFT)-calculated Gibbs free energy of adsorbed atomic hydrogen for nanoparticulate MoS_2 and the pure metals. Copyright 2007 Science.

5.1.1. Heteroatomic Doping

The introduction of heteroatoms can induce the redistribution of charges, resulting in different catalytic properties from perfect crystalline materials. In addition, heteroatom doping plays a vital role in generating complex defects and improving conductivity. Various heteroatom-doped Mo-based electrocatalysts have been designed with efficient performances in recent years. As early as 1984, Brown et al. discovered that alloys formed by transition metals (Fe, Co, Ni) doped into metallic Mo had excellent electrocatalytic hydrogen production performance [88]. Subsequent research found that compared to other Mo alloys, NiMo alloys had the best electrocatalytic activity, because Ni can regulate the electronic structure of Mo well. Gao et al. prepared porous Ni-Mo alloy microspheres grown directly on Cu foil via electrodeposition, as a highly efficient and durable catalyst for HER under alkaline conditions [69]. This unique self-supporting porous structure provided more active sites and improved

the conductivity of the electrode. The performance of the porous Ni-Mo alloy microspheres catalyst could be close to that of Pt/C. Interestingly, Nairan et al. reported a NiMo solid solution nanowire array electrode synthesized via a facile magnetic field assisted the growth process [89]. The doping of Mo atoms expanded the lattice of surface atoms (d-band shift), and thus, the intrinsic activity of the metal catalyst was significantly improved. This enhancement was also reasoned to be due to the presence of MoNi₄ phase and surface defect sites in the NiMo alloy. This electrocatalyst exhibited extremely small overpotential of 17 and 98 mV at 10 and 400 mA cm⁻², respectively, which were better than the majority of non-noble metal-based catalysts and even comparable to Pt/C electrodes [89].

In addition to elemental Mo, Mo-based compounds can also be doped with metal elements to form doping defects. For example, Lin and co-workers developed Co-doped Mo₂C nanowires by pyrolyzing metal complex precursor [72]. Co doping into the Mo₂C crystal structure increased the electron density near the Fermi level, resulting in a decrease of Mo-H intensity and promoting HER dynamics. Under the optimal Co/Mo ratio, the catalyst exhibited excellent HER performance and good stability in both alkaline and acidic electrolytes. This work strengthened the understanding of the electrocatalysis of carbide surfaces. In another study, Hu et al. used the molten salt method to prepare Ni-doped Mo₂C for the first time [18]. Compared to other transition metal carbides, Ni-doped Mo₂C showed excellent HER performance with a low overpotential of 121.4 mV (10 mA cm⁻²), which was due to possible electron transfer from Ni to Mo₂C, leading to a higher Ni valence and a lower Mo valence in the catalyst [90].

In addition to Mo carbides, metal-doped N-group, Mo-based compounds have also been designed for advanced electrocatalysts. N-group elements, Mo-based compounds primarily include Mo-based nitrides and phosphides. Among nitrides, Zhang et al. prepared Ni-doped MoN by plasma treatment, that gave NiMoN a layered porous structure, which not only provided a large electrode-electrolyte contact area, but also promoted the full transport of reactants and products [29]. Compared to the coating method, the electrodeposition method was applied on the carbon cloth, which brought the catalyst and the substrate into close contact and led to high stability during the electrolytic reaction. As a result of the synergy between bimetallic atoms, Ni-doped MoN exhibited properties close to commercial Pt/C [22,81]. In recent years, transition metal phosphides have shown excellent activity and stability in a wide pH medium, especially MoP doped with metal atoms. In one such investigation, Li et al. successfully prepared CoMoP nanorods with adjustable metallic valence [50]. This electrocatalyst displayed efficient activity toward HER, portraying the overpotential of 39 mV at 10 mA cm⁻² and a low Tafel slope of 73.3 mV per decade. The DFT calculations pinpointed that the H adsorption energy of the (013) and (211) planes of CoMoP was only 0.15 and -0.01 eV, which led to CoMoP exhibiting excellent HER performance.

Unlike most transition metal oxides, Mo oxide is a potential HER catalyst due to its high chemical stability and electrical conductivity. However, Mo oxide is easy to agglomerate during the preparation process, resulting in the reduction of exposed active sites. Therefore, metal atom doping has become one of the important ways to inhibit agglomeration and increase catalytic sites to enhance HER activity [91,92]. In a significant study, Xu et al. prepared CoNi-doped heterogeneous MoO₂ electrocatalysts for the first time using a one-step method [93]. This Co/Ni-MoO₂ composite showed a low overpotential of 103 mV (10 mA cm⁻²) in alkaline media due to the synergistic effect of heteroatoms and Mo. For a long time, MoS₂ was not considered a potential candidate because the bulk MoS₂ had low catalytic activity for HER. Interestingly, Hinnemann et al. found that the active site of MoS₂ was on the edge of the layered structure in 2005 [94]. Subsequently, the researchers used various methods to increase the edge of MoS₂ to improve the HER catalytic activity [95]. Among them, metal atom doping is an important method [3,82,96–100]. In one study, Dai et al. investigated metal-doped (Ni, Co, Fe) Mo sulfide and found that the HER performance was dominated by the nature of the metal M located in the M-MoS_x layered structure [96]. The CoMoS phase formed by Co doping provided synergistic regulation of the structure and electron distribution, which resulted in the formation of

many defects and active sites in CoMoS and enhanced the conductivity. This electrocatalyst exhibited excellent HER performance, with a low onset potential of 90 mV, and Tafel slope of 50 mV dec⁻¹.

Non-metallic elements, such as C, N, O, S, and Se atoms are abundant in valence electrons, which can significantly affect the catalytic properties of Mo-based materials. For example, one kind of O-doped MoS₂ was prepared by a one-step solvothermal method, in which dimethylformamide was used not only as a solvent, but also as a reducing agent and oxygen donor [48]. It was found that the doping of O atoms could modulate the electronic structure and vertical edge position of MoS₂, thereby enhancing the intrinsic conductivity of MoS₂. The O-doped MoS₂ exhibited excellent HER catalytic performance with an exceptionally small Tafel slope of 40 mV/decade and high current density of 20 mA/cm² at the overpotential of 200 mV due to the modulation of the electronic structure of MoS₂ via O atoms. Moreover, the doping of non-metallic atoms can change the crystalline phase of Mo-based materials, resulting in high catalytic activity. For example, Kwon and co-workers reported a non-stoichiometric Se-rich MoSe₂ synthesized by hydrothermal reaction [101]. When Se/Mo ratio exceeded two, the MoSe₂ changed from 2H to 1T' phase. Theoretical calculation results elucidated that Se-rich 1T' MoSe₂ exhibited a lower ΔG_{Hads} than 2H MoSe₂, which was conducive for enhancing HER performance. Se-rich MoSe₂ (with a Se/Mo ratio of 2.3) portrayed the best catalytic activity, which was consistent with the theoretical calculation results.

5.1.2. Vacancy Defects

Vacancy defects are one of the most common types of defects that could lead to substantial changes in the structure of Mo-based catalysts and adjust the charge distribution, conductivity, and active sites of the catalyst. As known, MoS₂ contains a large number of inert base planes and active edge sites. Therefore, activation of inactive base planes can greatly improve the catalytic properties of MoS₂. The introduction of S vacancies is of great significance for adjusting the electronic structure of the MoS₂ basal plane and thereby, improving HER catalytic activity.

In addition, the mismatch atomic radius between doping and intrinsic atoms may cause a new defect structure and increase the active sites density. In one study, Li et al. reported a method to form S vacancies in MoS₂ by doping with N atoms to enhance HER catalytic activity [28]. Theoretical calculation results showed that the ΔG_{Hads} value of pure MoS₂ was 2.11 eV, which is not good for HER. When N atoms were introduced to induce S vacancies in MoS₂, the exposed Mo atoms easily combined with H, and the ΔG_{Hads} value was only -0.63 eV. Nonetheless, the ΔG_{Hads} value on the N atom was -1.43 eV. These results highlighted that N doping only played a role in adjusting the electronic state density of S atoms in MoS₂, and N atoms were not active sites. Compared to pure MoS₂, N-doped MoS₂ possessed a low initial potential (-168 mV @10 mA cm⁻²) and Tafel slope (40.5 mV dec⁻¹). Similar results were also reported by Zhou group, where they found that the doping of carbon atoms not only increased the interlayer distance of MoS₂ but also enhanced the defects in the basal plane to expose more active sites [38].

The formation of S vacancies may induce the transformation of MoS₂ from a stable 2H phase to a metastable 1T phase. In an interesting study, Luo et al. found that Pd atoms in Pd-doped MoS₂ replaced some Mo sites in MoS₂, inducing the formation of S vacancies on the base planes, and simultaneously transforming MoS₂ from 2H into 1T phase [102]. Compared to the 2H phase, the HER activity of the 1T phase MoS₂ was higher [45], so this phase transition was beneficial to improve the HER performance of MoS₂. Theoretical calculations also demonstrated that the ΔG_{Hads} of S near the Pd site was only -0.02 eV, which highlighted that the introduction of Pd made part of S in the inert basal plane a new active site. The overpotential of MoS₂ was only 78 mV (10 mA/cm²), due to the generation of S active sites in the basal plane as well as the more edge active sites being exposed by the phase transition. Furthermore, S vacancy introduced in the basal plane of MoS₂ can also serve as an active site for HER [52]. For example, Meng et al. found that the ΔG_{Hads} value of laser treated MoS₂ (L-MoS₂) was only -0.17 eV, and the absolute value was less than that of pure MoS₂ [52]. At the same time, the generation of S vacancies regulated the electronic structure of MoS₂ and exposed

more uncoordinated Mo atoms to promote the intrinsic active sites. More exposure of Mo atoms was beneficial to enhance HER activity since Mo atoms were the active site of HER [95]. For another, Li and co-workers found that with the increase of S vacancies, more and more Mo atoms were exposed in the basal plane, and the catalytic activity of HER also kept increasing [103]. The appearance of S vacancies was also beneficial to increase the contact resistance of the catalyst and further enhance the HER catalytic activity [104].

O vacancies are another common point defect in Mo-based materials. Adding other active metals to the O-defect site is an effective method to enhance the HER activity of Mo-based oxides. Interestingly, Li et al. first obtained MoO₂ containing O defects via heat treatment, and then successfully anchored Pt nanoparticles to O vacancies by photoreduction [105]. Due to the doping of Pt atoms and the electronic regulation caused by O vacancies, the overpotential of Pt-doped MoO₂ was only 47 mV (10 mA cm⁻²). Similar research have also been reported by Mu's group [106]. Liu et al. constructed O vacancies in Ru-doped MoO₃ and found that the catalytic activity was enhanced as O vacancies increased.

Introducing proper Mo defects into Mo alloys can act in adjusting the catalytic performance of the alloys [107]. For instance, Li et al. synthesized a reverse opal-shaped MoC using a hard template method, in which many Mo vacancies were introduced during the template removal process. Theoretical and experimental results confirmed that Mo vacancies possessed a positive effect on HER performance [31].

5.1.3. Complex Defects

The currently reported synthesis strategies for defective catalysts are still difficult to control for specific types of defects [108]. Therefore, the majority of the defective electrocatalysts reported in the literature contain more than one type of defects, especially for multidimensional defects [109]. For example, Zhang et al. used arc melting to synthesize Mo oxide with various defects, in which the intensity of A-MoS₂ (after arc smelting) was significantly reduced in the PL spectrum, highlighting the formation of defects and cracks in MoS₂ [63]. Arc smelting not only caused various defects in MoS₂, but also changed the composition. A-MoS₂ exhibited excellent HER performance (low overpotential of 156 mV at 10 mA cm⁻² and a Tafel slope of 58 mV dec⁻¹), which may be caused by a combination of complex defects. In another study, Li et al. used liquid-exfoliated strategies to synthesize MoS₂ with a lot of surface and edge defects, and realized the doping of Au [110]. TEM images illustrated that the plane of the Au-doped MoS₂ layer exposed a large number of boundary edges and plane defects, which portrayed that this method does not synthesize a single defect. It was also observed that many defects and the doping of Au atoms played an active role in regulating the electronic structure of MoS₂. This catalyst demonstrated excellent HER performance with low overpotential (215 mV @ 10 mA cm⁻²) and Tafel slopes (58.2 mV dec⁻¹) due to the synergy of defects and Au atoms. Furthermore, researchers also reported many other types of complex defects and obtained satisfactory results for HER [30,57,71,76,111]. However, the study of the reaction mechanism of complex defects is still in the infant stage and requires holistic corroboration in the future.

Overall, defects play an important role in regulating the electron distribution on Mo-based materials, promoting electron transfer, and the adsorption of intermediates and reactants. The specific data for the application of HER in Mo-based catalyst defect engineering are comprehensively summarized in Table 1.

Table 1. Comparison of hydrogen evolution reaction (HER) performances of Mo-based defect electrocatalysts.

| Defects Type | Electrocatalysts | Electrolytes | Overpotential/mV | Tafel Slope (mV dec ⁻¹) | Ref. |
|----------------|---------------------------------------|--------------------------------------|----------------------------|-------------------------------------|------|
| Ni doping | Ni-Mo-S/C | pH = 7, PBS | 200@10 mA cm ⁻² | 48 | [3] |
| Heterojunction | MoO ₂ /a-Mo ₂ C | 1 M KOH | 100@10 mA cm ⁻² | 50 | [24] |
| Co doping | Co-MoS ₂ | 0.5 M H ₂ SO ₄ | 90@onset overpotential | 50 | [96] |

Table 1. Cont.

| Defects Type | Electrocatalysts | Electrolytes | Overpotential/mV | Tafel Slope (mV dec ⁻¹) | Ref. |
|-----------------|--|--------------------------------------|------------------------------|-------------------------------------|-------|
| S vacancy | MoS _x /CNTs | 0.5 M H ₂ SO ₄ | 106@10 mA cm ⁻² | 37 | [26] |
| O doping | O-MoS ₂ /rGO | 0.5 M H ₂ SO ₄ | 200@20 mA cm ⁻² | 40 | [48] |
| Complex defects | MoSe ₂ @CC | 0.5 M H ₂ SO ₄ | 182@10 mA cm ⁻² | 69 | [20] |
| Co doping | CoMoS | 1 M KOH | 98@10 mA cm ⁻² | 82 | [97] |
| Co doping | Co-NiMoN | 1 M KOH | 90@10 mA cm ⁻² | 72.2 | [112] |
| Co doping | CoMo-P/NF | 1 M KOH | 49@10 mA cm ⁻² | 36.28 | [27] |
| Ni doping | NiMo alloy | 2 M KOH | 65@10 mA cm ⁻² | 61.4 | [113] |
| Ni doping | NiMoO | 1 M KOH | 71@20 mA cm ⁻² | 57 | [44] |
| S vacancy | MoS ₂ -rGO | 0.5 M H ₂ SO ₄ | 168@10 mA cm ⁻² | 62 | [55] |
| Se doping | MoS ₂ (1-x)Se _{2x} | 0.5 M H ₂ SO ₄ | 164@10 mA cm ⁻² | 48 | [114] |
| Se rich | MoSe ₂ | 0.5 M H ₂ SO ₄ | 130@10 mA cm ⁻² | 46 | [101] |
| Mo vacancy | Mo _x C | 0.5 M H ₂ SO ₄ | 79@10 mA cm ⁻² | 60 | [31] |
| Complex defects | Mo ₂ C@2D-NPCs | 1 M KOH | 45@10 mA cm ⁻² | 46 | [115] |
| S vacancy | MoS ₂ | 0.5 M H ₂ SO ₄ | 178@10 mA cm ⁻² | 41.4 | [52] |
| S rich | MoS _{2.7} @NPG | 0.5 M H ₂ SO ₄ | 125@10 mA cm ⁻² | 41 | [116] |
| Complex defects | MoS ₂ @NPG | 0.5 M H ₂ SO ₄ | 118@onset overpotential | 46 | [117] |
| Complex defects | MoS ₂ | 0.5 M H ₂ SO ₄ | 120@onset overpotential | 50 | [70] |
| Co/Pd co-doping | Co/Pd-MoS ₂ | 0.5 M H ₂ SO ₄ | 49.3@10 mA cm ⁻² | 43.2 | [82] |
| Complex defects | MoS ₂ /NiS ₂ | 1 M KOH | 62@10 mA cm ⁻² | 50.1 | [60] |
| Complex defects | MoS ₂ /N-RGO | 0.5 M H ₂ SO ₄ | 56@10 mA cm ⁻² | 41.3 | [71] |
| Ni doping | NiMoN | 1 M KOH | 109@10 mA cm ⁻² | 95 | [29] |
| Co doping | Co-Mo ₂ C | 0.5 M H ₂ SO ₄ | 140@10 mA cm ⁻² | 39 | [72] |
| Ni doping | NiMo | 1 M KOH | 17@10 mA cm ⁻² | 43 | [89] |
| Complex defects | MoS ₂ /WS ₂ | 0.5 M H ₂ SO ₄ | 120@onset overpotential | 69 | [98] |
| Ni doping | NiMoN _x /C | 0.1 M HClO ₄ | 78@onset overpotential | 35.9 | [81] |
| N doping | N-MoP | 1 M KOH | 70@10 mA cm ⁻² | 55 | [40] |
| Complex defects | MoO ₂ @CoMo | 0.5 M H ₂ SO ₄ | 76@50 mA cm ⁻² | No report | [32] |
| Complex defects | MoS ₂ | 0.5 M H ₂ SO ₄ | 160@10 mA cm ⁻² | 46 | [62] |
| Complex defects | MoP/Mo | 0.5 M H ₂ SO ₄ | 224@10 mA cm ⁻² | No report | [17] |
| Heterojunction | Cu/Mo ₂ C/Mo ₂ N | 0.5 M H ₂ SO ₄ | 82@10 mA cm ⁻² | 33 | [118] |
| Complex defects | Ni/Mo ₂ C-PC | 1 M KOH | 179@10 mA cm ⁻² | 101 | [90] |
| O doping | O-Mo ₂ C | 1 M KOH | 132@10 mA cm ⁻² | 40 | [49] |
| Complex defects | MoS ₂ /C | 0.5 M H ₂ SO ₄ | 290@10 mA cm ⁻² | 80 | [108] |
| Ni doping | Ni-Mo ₂ C/C | 1 M KOH | 161@30 mA cm ⁻² | 73 | [68] |
| Ni doping | Ni-Mo ₂ C/CFP | 0.5 M H ₂ SO ₄ | 121.4@10 mA cm ⁻² | 116.9 | [18] |
| Ni doping | Ni-MoP/NF | 1 M KOH | 63@10 mA cm ⁻² | 97.3 | [119] |
| Complex defects | MoS ₂ /Mo | 0.5 M H ₂ SO ₄ | 120@onset overpotential | 46 | [30] |
| O doping | O-MoP | 0.5 M H ₂ SO ₄ | 156@10 mA cm ⁻² | 49 | [39] |
| O doping | O-MoS ₂ /CC | 0.5 M H ₂ SO ₄ | 90@onset overpotential | 58 | [120] |
| Co doping | CoMoP@NF | 1 M KOH | 39@10 mA cm ⁻² | 73.3 | [50] |
| Complex defects | MoS ₂ | 0.5 M H ₂ SO ₄ | 281@100 mA cm ⁻² | 43.6 | [121] |
| O doping | MoS ₂ | 0.5 M H ₂ SO ₄ | 120@onset overpotential | 55 | [122] |
| S vacancy | MoS ₂ | 0.5 M H ₂ SO ₄ | 153@10 mA cm ⁻² | 43 | [45] |
| S vacancy | MoS ₂ | 0.5 M H ₂ SO ₄ | 256@10 mA cm ⁻² | 93 | [123] |
| S doping | MoSe ₂ | 0.5 M H ₂ SO ₄ | 90@onset overpotential | 60 | [124] |
| O vacancy | α-MoO _{3-x} | 0.1 M KOH | 142@10 mA cm ⁻² | 58 | [23] |
| Ni doping | NiMo | 1 M KOH | 63@20 mA cm ⁻² | 49 | [69] |
| Complex defects | MoS ₂ /NCNFs | 0.5 M H ₂ SO ₄ | 135@10 mA cm ⁻² | 48 | [125] |
| Complex defects | O-MoS ₂ | 0.5 M H ₂ SO ₄ | 87@onset overpotential | 41 | [126] |
| Heterojunction | MoSe ₂ -Mo ₂ C | 1 M KOH | 51@10 mA cm ⁻² | 47.6 | [111] |
| Co doping | Co-Mo-S | 0.5 M H ₂ SO ₄ | 90@onset overpotential | 53 | [100] |
| N doping | N-a-MoC _{1-x} | 1 M KOH | 122@10 mA cm ⁻² | 39 | [41] |
| Ni doping | NiMoN | 1 M KOH | 89@10 mA cm ⁻² | No report | [127] |
| Complex defects | MoS ₂ | 0.5 M H ₂ SO ₄ | 118@onset overpotential | 51 | [76] |
| Complex defects | MoS ₂ | 0.5 M H ₂ SO ₄ | 172@10 mA cm ⁻² | 57 | [128] |
| Co doping | Co-MoS ₂ | 0.5 M H ₂ SO ₄ | 222@10 mA cm ⁻² | 64.2 | [129] |

Table 1. Cont.

| Defects Type | Electrocatalysts | Electrolytes | Overpotential/mV | Tafel Slope (mV dec ⁻¹) | Ref. |
|---------------------|------------------------|---------------------------------------|-----------------------------|-------------------------------------|-------|
| N doping | N-MoS ₂ | 0.5 M H ₂ SO ₄ | 168@10 mA cm ⁻² | 40.5 | [28] |
| S vacancy Pd doping | Pd-MoS ₂ | 0.5 M H ₂ SO ₄ | 106@10 mA cm ⁻² | 60 | [42] |
| Ni doping | Ni-MoP | 0.5 M H ₂ SO ₄ | 102@10 mA cm ⁻² | 58.1 | [130] |
| Complex defects | MoS ₂ /C | 0.05 M H ₂ SO ₄ | 103@onset overpotential | 56.1 | [77] |
| S vacancy | MoS ₂ | 0.5 M H ₂ SO ₄ | 170@10 mA cm ⁻² | 71 | [131] |
| Complex defects | MoS ₂ | 0.5 M H ₂ SO ₄ | 300@onset overpotential | 147 | [53] |
| S rich | MoS ₂ @SWNT | 0.5 M H ₂ SO ₄ | 92@onset overpotential | 41 | [83] |
| Complex defects | MoS ₂ -QDs | 0.5 M H ₂ SO ₄ | 187@100 mA cm ⁻² | 53 | [51] |
| S vacancy | MoS ₂ | 0.05 M H ₂ SO ₄ | 77@onset overpotential | 66 | [64] |
| Complex defects | MoS ₂ | 0.5 M H ₂ SO ₄ | 76@10 mA cm ⁻² | 47.4 | [132] |
| Complex defects | MoS ₂ | 0.5 M H ₂ SO ₄ | 85@onset overpotential | 78 | [61] |
| C-doping | C-MoS ₂ /GO | 0.5 M H ₂ SO ₄ | 165@onset overpotential | 46 | [38] |
| Complex defects | MoS ₂ /C | 0.5 M H ₂ SO ₄ | 503@onset overpotential | 95 | [133] |
| V doping | V-MoS ₂ | 1 M H ₂ SO ₄ | 130@10 mA cm ⁻² | 69 | [134] |
| Ni doping | Ni-Mo-N/CFC | 1 M KOH | 70@10 mA cm ⁻² | 70 | [22] |
| Ni doping | NiMoO ₄ /NF | 1 M KOH | 95@10 mA cm ⁻² | 82.1 | [91] |
| Complex defects | MoS ₂ | 0.1 M H ₂ SO ₄ | 40@onset overpotential | 63 | [135] |
| Complex defects | MoS ₂ | 0.5 M H ₂ SO ₄ | 80@onset overpotential | 90 | [136] |
| Complex defects | MoS ₂ | 0.5 M H ₂ SO ₄ | 176@10 mA cm ⁻² | 63 | [54] |
| Complex defects | MoS ₂ -RGO | 0.5 M H ₂ SO ₄ | 66@10 mA cm ⁻² | 38.6 | [137] |
| Complex defects | MoSe ₂ QDs | 0.5 M H ₂ SO ₄ | 120@onset overpotential | 67 | [56] |

5.2. Oxygen Evolution Reaction

OER is the other half reaction in the process of water decomposition, involving multiple electron transfers, and slow kinetic process. IrO₂ and RuO₂ are recognized as the most ideal OER catalysts, but their high cost limits the development of OER. Interestingly, Mo-based materials as non-noble catalysts have shown promising OER performance [60,69,90,112], but still a large performance gap compared to IrO₂ and RuO₂ exists. Therefore, well-designed defect engineering for Mo-based materials could be useful to improve the OER activity.

In an interesting investigation, Yin et al. synthesized Ni-doped MoN with MoO₃ as a precursor and used it as a bifunctional electrocatalyst [127]. It was observed from the HRTEM images that a large number of interfaces and complex defects appeared in NiMoN. Ni doping increased the intrinsic active sites of MoN, and also added new Ni active sites. Regulating structure of MoN via doped Ni resulted in MoN exhibiting excellent OER performance (overpotential only 295 mV at 10 mA cm⁻²). Additionally, NiMoO₄ with a large number of O vacancy defects has also been successfully synthesized and used to catalyze OER reactions [91]. In one such study, Zhang et al. found that as the content of oxygen vacancies increased, the catalytic activity of OER also increased. Theoretical calculation results confirmed that oxygen vacancies increased the adsorption energy of NiMoO₄ to water molecules, which was conducive for the full contact between water molecules and catalyst [91].

5.3. Oxygen Reduction Reaction

Fuel cells are one of the most hopeful technologies in sustainable energy conversion systems. However, the fuel cell's cathodic ORR kinetics is very slow, which greatly limits the energy output of the fuel cell. The design and preparation of ORR catalysts with high stability and activity to replace costly Pt has been a huge challenge over the years.

Doping is an effective strategy to enhance the ORR catalytic properties of Mo-based materials. For example, Cao et al. synthesized different stoichiometric MoN and Co-doped MoN and found that the doping of Co atoms transformed MoN into a hexagonal structure, as well as the presence of Mo³⁺ in this structure further enhanced ORR activity [138]. The co-doping of multi-atoms to regulate the ORR performance of Mo-based catalysts has attracted a lot of attention. For instance, one kind

of Mo-based compound co-doped with multi-atoms (Co, O, N, and C) was reported by the Khalifah group, in which the non-precious metal catalyst showed an excellent ORR activity under both acidic and alkaline conditions [139]. Among them, $\text{Co}_{0.5}\text{Mo}_{0.5}\text{O}_y\text{N}_z/\text{C}$ exhibited the best activity. During the synthesis process, Co formed Co-Mo bimetallic oxynitride, which possessed catalytic activity for ORR. This strategy of adjusting the metal oxidation state in the nitrogen oxide phase may lead to a further increase in ORR activity, approaching or even exceeding that of the Pt catalyst [139].

Furthermore, 2D nanocrystals with exposed high-energy facets have the expected high catalytic activity, but the synthesis process is difficult [140]. In one study, a metal MoO_2 with exposed high-energy (010) facet was successfully synthesized using the carbothermal reduction method. The obtained MoO_2 exposed almost 100% of the (010) plane, which significantly reduced the reaction barrier of the ORR. It was found that the atomic layer of MoO_2 had high electrocatalytic activity, good resistance to methanol, and good stability of ORR in alkaline electrolyte [141].

In recent years, researchers have discovered that M-N is the active site of the ORR reaction, so a series of M-N compounds have been synthesized. Lin et al. synthesized a N-doped C-supported Fe, Mo single-atom catalyst by pyrolyzing Fe, Mo bimetallic MOF (metal-organic frameworks) [142]. The doping of Mo atoms prevented the agglomeration of Fe and increased the active sites. Synergistic catalytic effect of Fe and Mo increased the degree of graphitization of carbon, so that carbon had a higher conductivity at a relatively low pyrolysis temperature. The (Fe, Mo)-N/C catalyst with Fe/Mo = 0.75 exhibited an excellent ORR performance.

5.4. Nitrogen Reduction Reaction

The synthetic ammonia (NH_3) industry is an important part of the current chemical industry, and the traditional Haber–Bosch method not only consumes large amount of energy, but also causes serious environmental pollution. The conversion of nitrogen molecules into NH_3 under mild conditions is an extremely attractive research area. Electrochemical nitrogen reduction (NRR) is the most promising method to achieve clean and sustainable NH_3 , as well as the process consumes low energy. Currently, the main challenge is to achieve high catalytic performance and high selectivity of the catalyst [143,144]. Since Mo is a very important component in biological nitrogenase, therefore it has become a research hotspot of NRR electrocatalysts. Moreover, several DFT calculations have also proved that Mo-based catalysts can promote the occurrence of the NRR [145]. In recent years, as understanding of defect sites has deepened, various defect-rich Mo-based materials have been synthesized and used in the catalytic process of NRR.

Constructing point defects is a common method to enhance the NRR catalytic performance of Mo-based materials. For example, Zhao et al. observed that the strong electronic interaction between Fe and MoS_2 significantly improved the NRR activity of Fe-doped MoS_2 [146]. Both theoretical calculations and experimental results corroborated that the high NRR activity of Fe- MoS_2 originated from the synergy between Fe and MoS_2 . Similar results were also reported by Chen's group [147]. Considering the low solubility of N_2 in water, Zeng et al. assembled a Co- $\text{MoS}_2/\text{N}@\text{C}$ nanomaterial with a hollow structure to promote mass transport. Due to its special nanostructure, Co- $\text{MoS}_2/\text{N}@\text{C}$ exhibited a high faradaic efficiency (FE) of 11.21% and a remarkable NH_3 yield rate of $129.93 \mu\text{g h}^{-1} \text{mg}_{\text{cat}}^{-1}$. In another interesting study, Zhang et al. reported an improved chemical vapor deposition method to controllably synthesize MoO_2 with different content of O vacancy defects, and its role in NRR process was comprehended [148]. The N_2 adsorption isotherm illustrated that the existence of O vacancies promoted the chemical adsorption of N_2 , thereby activating the $\text{N}\equiv\text{N}$ bond. Moreover, the density of states (DOS) calculations showed that O vacancies are also beneficial to the electron transfer in the catalytic process. This work emphasized that the proper introduction of vacancy defects can significantly improve the NRR, which is important for the design of different types of catalysts. Similarly, MoS_2 with both S vacancies and N doping defects was also used to catalyze the NRR reaction [149]. N doping produced a large number of S vacancies in MoS_2 , and at the same time, formed abundant Mo-N active sites which enhanced the FE (9.14%) and NH_3 yield ($69.82 \text{ mg h}^{-1} \text{mg}_{\text{cat}}^{-1}$).

Introduction of complex defects into Mo-based materials to enhance the catalytic property of NRR has also been reported, although it is not yet possible to precisely control the synthesis of complex defects. For example, Li et al. synthesized a MoS₂ nanoflower with complex defects. DFT calculations found that the existence of defects reduced the energy barrier of the rate-determining step, which was beneficial to promote the NRR. The experimental results also confirmed that complex defects afforded MoS₂ with ultra-high NRR catalytic performance, the FE could reach 8.34% and the yield rate of NH₃ reached 29.28 $\mu\text{g h}^{-1} \text{mg}^{-1} \text{cat}$. The activity of this defect-rich MoS₂ hardly decreased after seven cycles, highlighting that this catalyst possessed excellent stability. Table 2 shows a holistic summary of recently reported results of Mo-based materials defect engineering applied in OER and NRR.

Table 2. Summary of Mo-based defect electrocatalysts for oxygen evolution reaction (OER), oxygen reduction reaction (ORR), and electrochemical nitrogen reduction (NRR).

| Defects Type | Electrocatalysts | Electrolytes | Performance | Ref |
|------------------|--|--------------------------------------|--|-------|
| OER | | | | |
| Co doping | Co-MoNiN | 0.1 M KOH | Overpotential 365 mV @ 10 mA cm ⁻² , Tafel slop 73 mV dec ⁻¹ | [112] |
| Complex defects | MoS ₂ /NiS ₂ | 1 M KOH | Overpotential 360 mV @ 10 mA cm ⁻² | [60] |
| Ni doping | Ni-MoC/C | 1 M KOH | Overpotential 368 mV @ 10 mA cm ⁻² | [90] |
| Ni doping | NiMo | 1 M KOH | Overpotential 335 mV @ 10 mA cm ⁻² , Tafel slop 108 mV dec ⁻¹ | [69] |
| Ni doping | NiMoN | 1 M KOH | Overpotential 295 mV @ 10 mA cm ⁻² | [127] |
| Ni doping | Ni-MoO ₄ | 1 M KOH | Overpotential 310 mV @ 20 mA cm ⁻² , Tafel slop 42.3 mV dec ⁻¹ | [91] |
| Co doping | CoMoO ₄ | 1 M KOH | Overpotential 315 mV @ 10 mA cm ⁻² , Tafel slop 89 mV dec ⁻¹ | [150] |
| Ni-doping | NiMoO ₄ | 1 M KOH | Overpotential 340 mV @ 10 mA cm ⁻² , Tafel slop 45.6 mV dec ⁻¹ | [151] |
| Heterostructures | MoS ₂ /Ni ₃ S ₂ | 1 M KOH | Overpotential 218 mV @ 10 mA cm ⁻² , Tafel slop 88 mV dec ⁻¹ | [152] |
| Co doping | Co-MoO _x | 1 M KOH | Overpotential 340 mV @ 10 mA cm ⁻² , Tafel slop 49 mV dec ⁻¹ | [153] |
| ORR | | | | |
| Co doping | Co-NiMoN | 0.1 M KOH | Onset potential 0.89 V, half-wave potential 0.73 V, limited current density 4.3 mA cm ⁻² . | [112] |
| Complex defects | (Fe, Mo)-N/C | 0.5 M H ₂ SO ₄ | Onset potential 0.845 V, half-wave potential 0.674 V, limited current density 5.33 mA cm ⁻² . | [142] |

Table 2. Cont.

| Defects Type | Electrocatalysts | Electrolytes | Performance | Ref |
|--------------------------|--|---------------------------------------|---|-------|
| ORR | | | | |
| N doping | N-MoS ₂ /C | pH = 7.4, PBS | N-MoS ₂ /C-900 cathode achieves the maximum power density of 0.805 W m ⁻² | [154] |
| Multi atom doping | Co-Mo-O-N/C | 0.1 M KOH | onset potential 0.918 V vs. RHE, E _{half} = 0.758 V. | [139] |
| Co doping | Co _{0.6} Mo _{1.4} N ₂ | 0.1 M HClO ₄ | onset potential of 0.713 V | [138] |
| Co doping | Co _{0.5} Mo _{0.5} Ny/NCNC | 0.5 M H ₂ SO ₄ | onset potential of 0.808 V | [155] |
| Co, N co-doping | Co-N- MoO ₂ | 0.1 M KOH | onset potential of 0.87 V, overpotential 69 mV vs. RHE | [156] |
| Expose 010 crystal plane | MoO ₂ | 0.1 M KOH | kinetic current density of 8.47 mA cm ⁻² | [141] |
| NRR | | | | |
| Complex defects | MoS ₂ | 0.1 M Na ₂ SO ₄ | NH ₃ yield rate 29.28 μg h ⁻¹ mg ⁻¹ _{cat} . Faradaic efficiency of 8.34% | [65] |
| Complex defects | MoFe-PDC | 0.1 M HCl | NH ₃ yield rate 34.23 μg h ⁻¹ mg ⁻¹ _{cat} . Faradaic efficiency of 16.83% | [157] |
| Expose 110 crystal plane | Mo | 0.01 M H ₂ SO ₄ | NH ₃ yield rate 3.09 × 10 ⁻¹¹ mol s ⁻¹ cm ⁻² . Faradaic efficiency of 0.72% | [158] |
| Surface oxygen vacancies | MoO ₂ | 0.1 M HCl | NH ₃ yield rate ~12.20 μg h ⁻¹ mg ⁻¹ . Faradaic efficiency of 8.2% | [148] |
| S vacancy and N doping | N-MoS ₂ | 0.1 M Na ₂ SO ₄ | NH ₃ yield rate 69.82 mg h ⁻¹ mg _{cat} ⁻¹ . Faradaic efficiency of 9.14% | [149] |
| Mo doping | Mo-MnO ₂ | 0.1 M Na ₂ SO ₄ | NH ₃ yield rate 36.6 μg h ⁻¹ mg ⁻¹ . Faradaic efficiency of 12.1% | [159] |
| Co doping | Co-MoS ₂ | 0.1 M Na ₂ SO ₄ | NH ₃ yield rate 129.93 μg h ⁻¹ mg ⁻¹ _{cat} . Faradaic efficiency of 11.21% | [147] |
| Fe doping | Fe-MoS ₂ | 0.1 M KOH | NH ₃ yield rate 12.5 mg h ⁻¹ cm ⁻² . Faradaic efficiency of 10.8% | [146] |

6. Summary and Outlook

In summary, this review describes a variety of defect engineering strategies in Mo-based materials for enhanced electrocatalysis processes, including HER, OER, ORR, and NRR via redistributing electron density or serving as active sites of the electrocatalyst. In recent years, with the rapid development of advanced characterization techniques and theoretical calculations, researchers have proposed number of spatial defects of Mo-based materials that can enhance the kinetics of electrocatalysis. Although numerous works have been done in defect engineering of Mo-based materials for electrocatalysis, several challenges still deserve more attention as mentioned in the subsequent subsections.

(1) Precise control of defect synthesis

Although many reports have described the fine preparation processes of Mo-based defect-rich electrocatalysts, it is still a great challenge to precisely control the synthesis of defects. The detailed reaction mechanisms are different for different electrocatalytic reaction. Therefore, the ability to control the types, concentration, and distributions of various defect structures would enable the design of materials with tailored electrocatalytic performances. In addition, an ideal electrocatalyst should feature good activity as well as good cycling stability. Researchers often pay attention towards how to improve activity via designing fine defective structures but ignore the stability of defective structures under harsh conditions. Henceforth, precise control of synthetic defects with specific types, concentrations, locations, and stable structures may become the research direction of Mo-based defect electrocatalysts in the future.

(2) Investigations of complex defects

As elementary motifs of complex defects, point defects (vacancies and doping) have become a research focus for its relative easiness of synthesis, while hardly the effects of the complex defects in electrocatalytic reaction are reported. Complex defects, such as line defects (screw dislocation, edge dislocation), planar defects (grain boundary, twin boundary), and volume defects (void, disorder) have their distinct roles in the regulation of the electronic structure of electrocatalyst, which confers complex defects with maximum likelihood to enhance electrocatalytic performances. In addition, Schottky and Frenkel defects (a kind of unique point defect) have also been confirmed with unique electronic structures and physical properties. Therefore, with the gradual in-depth research on complex defects, the electrocatalytic performance of Mo-based materials should also be greatly improved.

(3) Understanding the mechanism of defect for electrocatalysis in-depth

Generally, defects can change the local electronic structure of the electrocatalyst to produce an unsaturated coordination state, which can serve as active site. However, several questions still need pondering: Are all the defects valuable? What kind of defects can improve catalytic performance? Will the defect structure change in the actual catalysis process? To what extent can defects improve performance? Due to the limitations of defect research, the answers to these questions are still vague. Therefore, some traditional and high-end in-situ characterization techniques should be combined to study the mechanism of defect catalysis. Additionally, more theoretical calculations and simulations should be conducted to guide the synthesis and analysis of defective electrocatalysts.

Author Contributions: G.Z. and X.G. searched the literature and wrote the manuscript draft; H.W. edited the literature; F.X., K.S., and S.Z. reviewed and helped to improve the content of the article. J.Y., L.Z., and M.S. done the conception, design and supervision. All authors reviewed the manuscript and agreed to the published version of the manuscript.

Funding: This work is supported by the National Key Research and Development Program of China (2017YFB0102900), the Research Grant Council (N_HKUST610/17) of the Hong Kong Special Administrative Region, and Shenzhen Science and Technology Innovation Committee (SGDX2019081623340748, JCYJ20180507183818040), Foshan-HKUST Project (FSUST19-FYTRI07), Hong Kong Branch of Southern Marine Science and Engineering Guangdong Laboratory (Guangzhou) (SMSEGL20SC01), Hong Kong Innovation and Technology Commission (grant no. ITC-CNERC14EG03, and ITC-CNERC14SC01), Jiangsu Key Laboratory for Chemistry of Low-Dimensional Materials (Grant no. JSKC19016).

Conflicts of Interest: The authors declare no conflict of interest.

References

1. Shao, M.; Chang, Q.; Dodelet, J.P.; Chenitz, R. Recent Advances in Electrocatalysts for Oxygen Reduction Reaction. *Chem. Rev.* **2016**, *116*, 3594–3657. [[CrossRef](#)] [[PubMed](#)]
2. Zhang, L.; Liu, W.; Dou, Y.; Du, Z.; Shao, M. The Role of Transition Metal and Nitrogen in Metal–N–C Composites for Hydrogen Evolution Reaction at Universal pHs. *J. Phys. Chem. C* **2016**, *120*, 29047–29053. [[CrossRef](#)]

3. Miao, J.; Xiao, F.; Yang, H.B.; Khoo, S.Y.; Chen, J.; Fan, Z.; Hsu, Y.; Chen, H.M.; Zhang, H.; Liu, B. Hierarchical Ni-Mo-S nanosheets on carbon fiber cloth: A flexible electrode for efficient hydrogen generation in neutral electrolyte. *Sci. Adv.* **2015**, *1*, 1500259. [[CrossRef](#)] [[PubMed](#)]
4. Zhang, J.; Bai, X.; Wang, T.; Xiao, W.; Xi, P.; Wang, J.; Gao, D.; Wang, J. Bimetallic Nickel Cobalt Sulfide as Efficient Electrocatalyst for Zn-Air Battery and Water Splitting. *Nanomicro Lett.* **2019**, *11*, 2. [[CrossRef](#)] [[PubMed](#)]
5. Lian, Y.; Yang, W.; Zhang, C.; Sun, H.; Deng, Z.; Xu, W.; Song, L.; Ouyang, Z.; Wang, Z.; Guo, J.; et al. Unpaired 3d Electrons on Atomically Dispersed Cobalt Centres in Coordination Polymers Regulate both Oxygen Reduction Reaction (ORR) Activity and Selectivity for Use in Zinc-Air Batteries. *Angew. Chem. Int. Ed. Engl.* **2020**, *59*, 286–294. [[CrossRef](#)]
6. Shao, M. Electrocatalysis in Fuel Cells. *Catalysts* **2015**, *5*, 2115–2121. [[CrossRef](#)]
7. Zeng, H.; Chen, S.; Jin, Y.; Li, J.; Song, J.; Le, Z.; Liang, G.; Zhang, H.; Xie, F.; Chen, J.; et al. Electron Density Modulation of Metallic MoO₂ by Ni Doping to Produce Excellent Hydrogen Evolution and Oxidation Activities in Acid. *ACS Energy Lett.* **2020**, *5*, 1908–1915. [[CrossRef](#)]
8. Jiao, Y.; Zheng, Y.; Jaroniec, M.; Qiao, S.Z. Design of electrocatalysts for oxygen- and hydrogen-involving energy conversion reactions. *Chem. Soc. Rev.* **2015**, *44*, 2060–2086. [[CrossRef](#)]
9. Jia, Y.; Jiang, K.; Wang, H.; Yao, X. The Role of Defect Sites in Nanomaterials for Electrocatalytic Energy Conversion. *Chem* **2019**, *5*, 1371–1397. [[CrossRef](#)]
10. Stamenkovic, V.R.; Strmcnik, D.; Lopes, P.P.; Markovic, N.M. Energy and fuels from electrochemical interfaces. *Nat. Mater.* **2016**, *16*, 57–69. [[CrossRef](#)]
11. Seh, Z.W.; Kibsgaard, J.; Dickens, C.F.; Chorkendorff, I.; Norskov, J.K.; Jaramillo, T.F. Combining theory and experiment in electrocatalysis: Insights into materials design. *Science* **2017**, *355*, 4998. [[CrossRef](#)] [[PubMed](#)]
12. Liu, M.; Pang, Y.; Zhang, B.; De Luna, P.; Voznyy, O.; Xu, J.; Zheng, X.; Dinh, C.T.; Fan, F.; Cao, C.; et al. Enhanced electrocatalytic CO₂ reduction via field-induced reagent concentration. *Nature* **2016**, *537*, 382–386. [[CrossRef](#)] [[PubMed](#)]
13. Peles, A.; Shao, M.; Protsailo, L. Pt Monolayer Electrocatalyst for Oxygen Reduction Reaction on Pd-Cu Alloy: First-Principles Investigation. *Catalysts* **2015**, *5*, 1193–1201. [[CrossRef](#)]
14. Xu, X.; Tian, X.; Sun, B.; Liang, Z.; Cui, H.; Tian, J.; Shao, M. 1 T-phase molybdenum sulfide nanodots enable efficient electrocatalytic nitrogen fixation under ambient conditions. *Appl. Catal. B Environ.* **2020**, *272*, 118984. [[CrossRef](#)]
15. Sun, D.; Huang, D.; Wang, H.; Xu, G.; Zhang, X.; Zhang, R.; Tang, Y.; Abd Ei-Hady, D.; Alshitari, W.; Saad Al-Bogami, A.; et al. 1T MoS₂ nanosheets with extraordinary sodium storage properties via thermal-driven ion intercalation assisted exfoliation of bulky MoS₂. *Nano Energy* **2019**, *61*, 361–369. [[CrossRef](#)]
16. Ren, J.; Chen, L.; Weng, C.; Yuan, Z. Ultrafine molybdenum phosphide nanocrystals on a highly porous N,P-codoped carbon matrix as an efficient catalyst for the hydrogen evolution reaction. *Mater. Chem. Front.* **2018**, *2*, 1987–1996. [[CrossRef](#)]
17. Yu, H.; Cao, S.; Fu, B.; Wu, Z.; Liu, J.; Piao, L. Self-supported nanotubular MoP electrode for highly efficient hydrogen evolution via water splitting. *Catal. Commun.* **2019**, *127*, 1–4. [[CrossRef](#)]
18. Hu, Z.; Huang, J.; Luo, Y.; Liu, M.; Li, X.; Yan, M.; Ye, Z.; Chen, Z.; Feng, Z.; Huang, S. Wrinkled Ni-doped Mo₂C coating on carbon fiber paper: An advanced electrocatalyst prepared by molten-salt method for hydrogen evolution reaction. *Electrochim. Acta* **2019**, *319*, 293–301. [[CrossRef](#)]
19. Song, Y.; Ren, J.; Yuan, G.; Yao, Y.; Liu, X.; Yuan, Z. Facile synthesis of Mo₂C nanoparticles on N-doped carbon nanotubes with enhanced electrocatalytic activity for hydrogen evolution and oxygen reduction reactions. *J. Energy Chem.* **2019**, *38*, 68–77. [[CrossRef](#)]
20. Qu, B.; Yu, X.; Chen, Y.; Zhu, C.; Li, C.; Yin, Z.; Zhang, X. Ultrathin MoSe₂ Nanosheets Decorated on Carbon Fiber Cloth as Binder-Free and High-Performance Electrocatalyst for Hydrogen Evolution. *ACS Appl. Mater. Interfaces* **2015**, *7*, 14170–14175. [[CrossRef](#)]
21. Rauscher, T.; Müller, C.I.; Schmidt, A.; Kieback, B.; Röntzsch, L. Ni-Mo-B alloys as cathode material for alkaline water electrolysis. *Int. J. Hydrogen Energy* **2016**, *41*, 2165–2176. [[CrossRef](#)]
22. Li, Y.; Wei, X.; Chen, L.; Shi, J.; He, M. Nickel-molybdenum nitride nanoplate electrocatalysts for concurrent electrolytic hydrogen and formate productions. *Nat. Commun.* **2019**, *10*, 5335. [[CrossRef](#)] [[PubMed](#)]

23. Datta, R.S.; Haque, F.; Mohiuddin, M.; Carey, B.J.; Syed, N.; Zavabeti, A.; Zhang, B.; Khan, H.; Berean, K.J.; Ou, J.Z.; et al. Highly active two dimensional α -MoO_{3-x} for the electrocatalytic hydrogen evolution reaction. *J. Mater. Chem. A* **2017**, *5*, 24223–24231. [[CrossRef](#)]
24. Liu, Y.; Huang, B.; Xie, Z. Hydrothermal synthesis of core-shell MoO₂/Mo₂C heterojunction as high performance electrocatalyst for hydrogen evolution reaction. *Appl. Surf. Sci.* **2018**, *427*, 693–701. [[CrossRef](#)]
25. Chen, S.; Duan, J.; Tang, Y.; Jin, B.; Zhangiao, S. Molybdenum sulfide clusters-nitrogen-doped graphene hybrid hydrogel film as an efficient three-dimensional hydrogen evolution electrocatalyst. *Nano Energy* **2015**, *11*, 11–18. [[CrossRef](#)]
26. Li, P.; Yang, Z.; Shen, J.; Nie, H.; Cai, Q.; Li, L.; Ge, M.; Gu, C.; Chen, X.; Yang, K.; et al. Subnanometer Molybdenum Sulfide on Carbon Nanotubes as a Highly Active and Stable Electrocatalyst for Hydrogen Evolution Reaction. *ACS Appl. Mater. Interfaces* **2016**, *8*, 3543–3550. [[CrossRef](#)]
27. Han, Y.; Li, P.; Tian, Z.; Zhang, C.; Ye, Y.; Zhu, X.; Liang, C. Molybdenum-Doped Porous Cobalt Phosphide Nanosheets for Efficient Alkaline Hydrogen Evolution. *ACS Appl. Energy Mater.* **2019**, *2*, 6302–6310. [[CrossRef](#)]
28. Li, R.; Yang, L.; Xiong, T.; Wu, Y.; Cao, L.; Yuan, D.; Zhou, W. Nitrogen doped MoS₂ nanosheets synthesized via a low-temperature process as electrocatalysts with enhanced activity for hydrogen evolution reaction. *J. Power Sources* **2017**, *356*, 133–139. [[CrossRef](#)]
29. Zhang, Y.; Ouyang, B.; Xu, J.; Chen, S.; Rawat, R.S.; Fan, H.J. 3D Porous Hierarchical Nickel-Molybdenum Nitrides Synthesized by RF Plasma as Highly Active and Stable Hydrogen-Evolution-Reaction Electrocatalysts. *Adv. Energy Mater.* **2016**, *6*, 1600221. [[CrossRef](#)]
30. Xu, Y.; Zheng, C.; Wang, S.; Hou, Y. 3D arrays of molybdenum sulphide nanosheets on Mo meshes: Efficient electrocatalysts for hydrogen evolution reaction. *Electrochim. Acta* **2015**, *174*, 653–659. [[CrossRef](#)]
31. Li, F.; Zhao, X.; Mahmood, J.; Okyay, M.S.; Jung, S.M.; Ahmad, I.; Kim, S.J.; Han, G.F.; Park, N.; Baek, J.B. Macroporous Inverse Opal-like Mo_xC with Incorporated Mo Vacancies for Significantly Enhanced Hydrogen Evolution. *ACS Nano* **2017**, *11*, 7527–7533. [[CrossRef](#)] [[PubMed](#)]
32. Han, G.H.; Kim, H.; Kim, J.; Kim, J.; Kim, S.Y.; Ahn, S.H. Micro-nanoporous MoO₂@CoMo heterostructure catalyst for hydrogen evolution reaction. *Appl. Catal. B Environ.* **2020**, *270*, 118895. [[CrossRef](#)]
33. Huang, Y.; Yang, T.; Yang, L.; Liu, R.; Zhang, G.; Jiang, J.; Luo, Y.; Lian, P.; Tang, S. Graphene-boron nitride hybrid-supported single Mo atom electrocatalysts for efficient nitrogen reduction reaction. *J. Mater. Chem. A* **2019**, *7*, 15173–15180. [[CrossRef](#)]
34. Lei, Y.; Yang, Y.; Liu, Y.; Zhu, Y.; Jia, M.; Zhang, Y.; Zhang, K.; Yu, A.; Liu, J.; Zhai, J. Nitrogen-Doped Porous Carbon Nanosheets Strongly Coupled with Mo₂C Nanoparticles for Efficient Electrocatalytic Hydrogen Evolution. *Nanoscale Res. Lett.* **2019**, *14*, 329. [[CrossRef](#)] [[PubMed](#)]
35. Kong, X.; Peng, H.; Bu, S.; Gao, Q.; Jiao, T.; Cheng, J.; Liu, B.; Hong, G.; Lee, C.; Zhang, W. Defect engineering of nanostructured electrocatalysts for enhancing nitrogen reduction. *J. Mater. Chem. A* **2020**, *8*, 7457–7473. [[CrossRef](#)]
36. Wang, Y.; Han, P.; Lv, X.; Zhang, L.; Zheng, G. Defect and Interface Engineering for Aqueous Electrocatalytic CO₂ Reduction. *Joule* **2018**, *2*, 2551–2582. [[CrossRef](#)]
37. Yan, X.; Jia, Y.; Yao, X. Defects on carbons for electrocatalytic oxygen reduction. *Chem. Soc. Rev.* **2018**, *47*, 7628–7658. [[CrossRef](#)]
38. Li, Y.; Wang, J.; Tian, X.; Ma, L.; Dai, C.; Yang, C.; Zhou, Z. Carbon doped molybdenum disulfide nanosheets stabilized on graphene for the hydrogen evolution reaction with high electrocatalytic ability. *Nanoscale* **2016**, *8*, 1676–1683. [[CrossRef](#)]
39. Zhang, X.; Wu, Z.; Wang, D. Oxygen-incorporated defect-rich MoP for highly efficient hydrogen production in both acidic and alkaline media. *Electrochim. Acta* **2018**, *281*, 540–548. [[CrossRef](#)]
40. Chen, N.; Zhang, W.; Zeng, J.; He, L.; Li, D.; Gao, Q. Plasma-Engineered MoP with nitrogen doping: Electron localization toward efficient alkaline hydrogen evolution. *Appl. Catal. B Environ.* **2020**, *268*. [[CrossRef](#)]
41. Tang, C.; Zhang, H.; Xu, K.; Zhang, Q.; Liu, J.; He, C.; Fan, L.; Asefa, T. Unconventional molybdenum carbide phases with high electrocatalytic activity for hydrogen evolution reaction. *J. Mater. Chem. A* **2019**, *7*, 18030–18038. [[CrossRef](#)]
42. Zhao, Y.; Hwang, J.; Tang, M.T.; Chun, H.; Wang, X.; Zhao, H.; Chan, K.; Han, B.; Gao, P.; Li, H. Ultrastable molybdenum disulfide-based electrocatalyst for hydrogen evolution in acidic media. *J. Power Sources* **2020**, *456*, 227998. [[CrossRef](#)]

43. Tong, Y.; Chen, P.; Zhang, M.; Zhou, T.; Zhang, L.; Chu, W.; Wu, C.; Xie, Y. Oxygen Vacancies Confined in Nickel Molybdenum Oxide Porous Nanosheets for Promoted Electrocatalytic Urea Oxidation. *ACS Catal.* **2017**, *8*, 1–7. [[CrossRef](#)]
44. Zhu, Y.a.; Pan, Y.; Dai, W.; Lu, T. Dealloying Generation of Oxygen Vacancies in the Amorphous Nanoporous Ni–Mo–O for Superior Electrocatalytic Hydrogen Generation. *ACS Appl. Energy Mater.* **2020**, *3*, 1319–1327. [[CrossRef](#)]
45. Yin, Y.; Han, J.; Zhang, Y.; Zhang, X.; Xu, P.; Yuan, Q.; Samad, L.; Wang, X.; Wang, Y.; Zhang, Z.; et al. Contributions of Phase, Sulfur Vacancies, and Edges to the Hydrogen Evolution Reaction Catalytic Activity of Porous Molybdenum Disulfide Nanosheets. *J. Am. Chem. Soc.* **2016**, *138*, 7965–7972. [[CrossRef](#)] [[PubMed](#)]
46. Li, D.J.; Maiti, U.N.; Lim, J.; Choi, D.S.; Lee, W.J.; Oh, Y.; Lee, G.Y.; Kim, S.O. Molybdenum sulfide/N-doped CNT forest hybrid catalysts for high-performance hydrogen evolution reaction. *Nano Lett.* **2014**, *14*, 1228–1233. [[CrossRef](#)] [[PubMed](#)]
47. Zhang, K.; Kim, H.J.; Lee, J.T.; Chang, G.W.; Shi, X.; Kim, W.; Ma, M.; Kong, K.J.; Choi, J.M.; Song, M.S.; et al. Unconventional pore and defect generation in molybdenum disulfide: Application in high-rate lithium-ion batteries and the hydrogen evolution reaction. *ChemSusChem* **2014**, *7*, 2489–2495. [[CrossRef](#)] [[PubMed](#)]
48. Liu, A.; Zhao, L.; Zhang, J.; Lin, L.; Wu, H. Solvent-Assisted Oxygen Incorporation of Vertically Aligned MoS₂ Ultrathin Nanosheets Decorated on Reduced Graphene Oxide for Improved Electrocatalytic Hydrogen Evolution. *ACS Appl. Mater. Interfaces* **2016**, *8*, 25210–25218. [[CrossRef](#)]
49. Yang, H.; Chen, X.; Hu, G.; Chen, W.; Bradley, S.J.; Zhang, W.; Verma, G.; Nann, T.; Jiang, D.; Kruger, P.E.; et al. Highly efficient electrocatalytic hydrogen evolution promoted by O–Mo–C interfaces of ultrafine β-Mo₂C nanostructures. *Chem. Sci.* **2020**, *11*, 3523–3530. [[CrossRef](#)]
50. Li, D.; Liu, D.; Zhao, S.; Lu, S.; Ma, Y.; Li, M.; Chen, G.; Wang, Y.; Zhou, G.; Xiao, C. Tuning of metallic valence in CoMoP for promoting electrocatalytic hydrogen evolution. *Int. J. Hydrogen Energy* **2019**, *44*, 31072–31081. [[CrossRef](#)]
51. Ou, G.; Fan, P.; Ke, X.; Xu, Y.; Huang, K.; Wei, H.; Yu, W.; Zhang, H.; Zhong, M.; Wu, H.; et al. Defective molybdenum sulfide quantum dots as highly active hydrogen evolution electrocatalysts. *Nano Res.* **2017**, *11*, 751–761. [[CrossRef](#)]
52. Meng, C.; Lin, M.; Du, X.; Zhou, Y. Molybdenum Disulfide Modified by Laser Irradiation for Catalyzing Hydrogen Evolution. *ACS Sustain. Chem. Eng.* **2019**, *7*, 6999–7003. [[CrossRef](#)]
53. Ye, G.; Gong, Y.; Lin, J.; Li, B.; He, Y.; Pantelides, S.T.; Zhou, W.; Vajtai, R.; Ajayan, P.M. Defects Engineered Monolayer MoS₂ for Improved Hydrogen Evolution Reaction. *Nano Lett.* **2016**, *16*, 1097–1103. [[CrossRef](#)] [[PubMed](#)]
54. Zhang, L.; Ke, X.; Ou, G.; Wei, H.; Wang, L.; Wu, H. Defective MoS₂ electrocatalyst for highly efficient HER through a simple balling milling method. *Sci. China Mater.* **2017**, *60*, 849–856. [[CrossRef](#)]
55. Mondal, A.; Paul, A.; Srivastava, D.N.; Panda, A.B. Defect- and Phase-Induced Acceleration of Electrocatalytic Hydrogen Production by Ultrathin and Small MoS₂-Decorated rGO Sheets. *ACS Appl. Nano Mater.* **2018**, *1*, 4622–4632. [[CrossRef](#)]
56. Zhu, C.; Huang, Y.; Xu, F.; Gao, P.; Ge, B.; Chen, J.; Zeng, H.; Sutter, E.; Sutter, P.; Sun, L. Defect-Laden MoSe₂ Quantum Dots Made by Turbulent Shear Mixing as Enhanced Electrocatalysts. *Small* **2017**, *13*, 1700565. [[CrossRef](#)]
57. Sarker, S.; Peters, J.; Chen, X.; Li, B.; Chen, G.; Yan, L.; Richins, S.K.; Das, S.; Zhou, M.; Luo, H. Engineering Molybdenum Diselenide and Its Reduced Graphene Oxide Hybrids for Efficient Electrocatalytic Hydrogen Evolution. *ACS Appl. Nano Mater.* **2018**, *1*, 2143–2152. [[CrossRef](#)]
58. Lu, A.Y.; Yang, X.; Tseng, C.C.; Min, S.; Lin, S.H.; Hsu, C.L.; Li, H.; Idriss, H.; Kuo, J.L.; Huang, K.W.; et al. High-Sulfur-Vacancy Amorphous Molybdenum Sulfide as a High Current Electrocatalyst in Hydrogen Evolution. *Small* **2016**, *12*, 5530–5537. [[CrossRef](#)]
59. Wang, X.; Zhang, Y.; Si, H.; Zhang, Q.; Wu, J.; Gao, L.; Wei, X.; Sun, Y.; Liao, Q.; Zhang, Z.; et al. Single-Atom Vacancy Defect to Trigger High-Efficiency Hydrogen Evolution of MoS₂. *J. Am. Chem. Soc.* **2020**, *142*, 4298–4308. [[CrossRef](#)]
60. Lin, J.; Wang, P.; Wang, H.; Li, C.; Si, X.; Qi, J.; Cao, J.; Zhong, Z.; Fei, W.; Feng, J. Defect-Rich Heterogeneous MoS₂/NiS₂ Nanosheets Electrocatalysts for Efficient Overall Water Splitting. *Adv. Sci.* **2019**, *6*, 1900246. [[CrossRef](#)]

61. Xie, J.; Qu, H.; Xin, J.; Zhang, X.; Cui, G.; Zhang, X.; Bao, J.; Tang, B.; Xie, Y. Defect-rich MoS₂ nanowall catalyst for efficient hydrogen evolution reaction. *Nano Res.* **2017**, *10*, 1178–1188. [[CrossRef](#)]
62. Li, Y.; Yin, K.; Wang, L.; Lu, X.; Zhang, Y.; Liu, Y.; Yan, D.; Song, Y.; Luo, S. Engineering MoS₂ nanomesh with holes and lattice defects for highly active hydrogen evolution reaction. *Appl. Catal. B Environ.* **2018**, *239*, 537–544. [[CrossRef](#)]
63. Zhang, L.; Ou, G.; Gu, L.; Peng, Z.; Wang, L.; Wu, H. A highly active molybdenum multisulfide electrocatalyst for the hydrogen evolution reaction. *RSC Adv.* **2016**, *6*, 107158–107162. [[CrossRef](#)]
64. Sun, C.; Wang, P.; Wang, H.; Xu, C.; Zhu, J.; Liang, Y.; Su, Y.; Jiang, Y.; Wu, W.; Fu, E.; et al. Defect engineering of molybdenum disulfide through ion irradiation to boost hydrogen evolution reaction performance. *Nano Res.* **2019**, *12*, 1613–1618. [[CrossRef](#)]
65. Li, X.; Li, T.; Ma, Y.; Wei, Q.; Qiu, W.; Guo, H.; Shi, X.; Zhang, P.; Asiri, A.M.; Chen, L.; et al. Boosted Electrocatalytic N₂ Reduction to NH₃ by Defect-Rich MoS₂ Nanoflower. *Adv. Energy Mater.* **2018**, *8*. [[CrossRef](#)]
66. Hage, F.S.; Radtke, G.; Kepaptsoglou, D.M.; Lazzeri, M.; Ramasse, Q.M. Single-atom vibrational spectroscopy in the scanning transmission electron microscope. *Science* **2020**, *367*, 1124–1127. [[CrossRef](#)] [[PubMed](#)]
67. Kwon, I.S.; Debela, T.T.; Kwak, I.H.; Park, Y.C.; Seo, J.; Shim, J.Y.; Yoo, S.J.; Kim, J.-G.; Park, J.; Kang, H.S. Ruthenium Nanoparticles on Cobalt-Doped 1T' Phase MoS₂ Nanosheets for Overall Water Splitting. *Small* **2020**, *16*, 2000081. [[CrossRef](#)]
68. Sun, L.; Wang, C.; Sun, Q.; Cheng, Y.; Wang, L. Self-Assembly of Hierarchical Ni-Mo-Polydopamine Microflowers and their Conversion to a Ni-Mo₂C/C Composite for Water Splitting. *Chem. Eur. J.* **2017**, *23*, 4644–4650. [[CrossRef](#)]
69. Gao, M.Y.; Yang, C.; Zhang, Q.B.; Zeng, J.R.; Li, X.T.; Hua, Y.X.; Xu, C.Y.; Dong, P. Facile electrochemical preparation of self-supported porous Ni–Mo alloy microsphere films as efficient bifunctional electrocatalysts for water splitting. *J. Mater. Chem. A* **2017**, *5*, 5797–5805. [[CrossRef](#)]
70. Xie, J.; Zhang, H.; Li, S.; Wang, R.; Sun, X.; Zhou, M.; Zhou, J.; Lou, X.W.; Xie, Y. Defect-rich MoS₂ ultrathin nanosheets with additional active edge sites for enhanced electrocatalytic hydrogen evolution. *Adv. Mater.* **2013**, *25*, 5807–5813. [[CrossRef](#)]
71. Tang, Y.; Wang, Y.; Wang, X.; Li, S.; Huang, W.; Dong, L.; Liu, C.; Li, Y.; Lan, Y. Molybdenum Disulfide/Nitrogen-Doped Reduced Graphene Oxide Nanocomposite with Enlarged Interlayer Spacing for Electrocatalytic Hydrogen Evolution. *Adv. Energy Mater.* **2016**, *6*, 1600116. [[CrossRef](#)]
72. Lin, H.; Liu, N.; Shi, Z.; Guo, Y.; Tang, Y.; Gao, Q. Cobalt-Doping in Molybdenum-Carbide Nanowires Toward Efficient Electrocatalytic Hydrogen Evolution. *Adv. Funct. Mater.* **2016**, *26*, 5590–5598. [[CrossRef](#)]
73. Staszak-Jirkovsky, J.; Malliakas, C.D.; Lopes, P.P.; Danilovic, N.; Kota, S.S.; Chang, K.C.; Genorio, B.; Strmcnik, D.; Stamenkovic, V.R.; Kanatzidis, M.G.; et al. Design of active and stable Co-Mo-S_x chalcogenides as pH-universal catalysts for the hydrogen evolution reaction. *Nat. Mater.* **2016**, *15*, 197–203. [[CrossRef](#)] [[PubMed](#)]
74. Sun, Z.; He, J.; Yuan, M.; Lin, L.; Zhang, Z.; Kang, Z.; Liao, Q.; Li, H.; Sun, G.; Yang, X.; et al. Li⁺-clipping for edge S-vacancy MoS₂ quantum dots as an efficient bifunctional electrocatalyst enabling discharge growth of amorphous Li₂O₂ film. *Nano Energy* **2019**, *65*, 103996. [[CrossRef](#)]
75. Yu, X.Y.; Hu, H.; Wang, Y.; Chen, H.; Lou, X.W. Ultrathin MoS₂ Nanosheets Supported on N-doped Carbon Nanoboxes with Enhanced Lithium Storage and Electrocatalytic Properties. *Angew. Chem. Int. Ed.* **2015**, *54*, 7395–7398. [[CrossRef](#)] [[PubMed](#)]
76. Lin, Q.; Dong, X.; Wang, Y.; Zheng, N.; Zhao, Y.; Xu, W.; Ding, T. Molybdenum disulfide with enlarged interlayer spacing decorated on reduced graphene oxide for efficient electrocatalytic hydrogen evolution. *J. Mater. Sci.* **2020**, *55*, 6637–6647. [[CrossRef](#)]
77. Yang, L.; Zhou, W.; Lu, J.; Hou, D.; Ke, Y.; Li, G.; Tang, Z.; Kang, X.; Chen, S. Hierarchical spheres constructed by defect-rich MoS₂/carbon nanosheets for efficient electrocatalytic hydrogen evolution. *Nano Energy* **2016**, *22*, 490–498. [[CrossRef](#)]
78. Zhou, G.; Yin, J.; Sun, Z.; Gao, X.; Zhu, F.; Zhao, P.; Li, R.; Xu, J. An ultrasonic-assisted synthesis of rice-straw-based porous carbon with high performance symmetric supercapacitors. *RSC Adv.* **2020**, *10*, 3246–3255. [[CrossRef](#)]

79. Kang, S.; Koo, J.; Seo, H.; Truong, Q.T.; Park, J.B.; Park, S.C.; Jung, Y.; Cho, S.; Nam, K.T.; Kim, Z.H.; et al. Defect-engineered MoS₂ with extended photoluminescence lifetime for high-performance hydrogen evolution. *J. Mater. Chem. C* **2019**, *7*, 10173–10178. [[CrossRef](#)]
80. Ganesh, R.S.; Durgadevi, E.; Silambarasan, K.; Navaneethan, M.; Ponnusamy, S.; Kong, C.Y.; Muthamizhchelvan, C.; Shimura, Y.; Hayakawa, Y. Effect of ethylenediamine on morphology of 2D Co-Mo-S@NG hybrids and their enhanced electrocatalytic activity for DSSCs application. *Mater. Sci. Semicond. Proc.* **2020**, *105*, 104725. [[CrossRef](#)]
81. Chen, W.F.; Sasaki, K.; Ma, C.; Frenkel, A.I.; Marinkovic, N.; Muckerman, J.T.; Zhu, Y.; Adzic, R.R. Hydrogen-evolution catalysts based on non-noble metal nickel-molybdenum nitride nanosheets. *Angew. Chem. Int. Ed.* **2012**, *51*, 6131–6135. [[CrossRef](#)] [[PubMed](#)]
82. Yang, W.; Zhang, S.; Chen, Q.; Zhang, C.; Wei, Y.; Jiang, H.; Lin, Y.; Zhao, M.; He, Q.; Wang, X.; et al. Conversion of Intercalated MoO₃ to Multi-Heteroatoms-Doped MoS₂ with High Hydrogen Evolution Activity. *Adv. Mater.* **2020**. [[CrossRef](#)]
83. Liu, D.; Xu, W.; Liu, Q.; He, Q.; Haleem, Y.A.; Wang, C.; Xiang, T.; Zou, C.; Chu, W.; Zhong, J.; et al. Unsaturated-sulfur-rich MoS₂ nanosheets decorated on free-standing SWNT film: Synthesis, characterization and electrocatalytic application. *Nano Res.* **2016**, *9*, 2079–2087. [[CrossRef](#)]
84. Yang, W.; Chen, S. Recent progress in electrode fabrication for electrocatalytic hydrogen evolution reaction: A mini review. *Chem. Eng. J.* **2020**, *393*, 124726. [[CrossRef](#)]
85. Theerthagiri, J.; Lee, S.J.; Murthy, A.P.; Madhavan, J.; Choi, M.Y. Fundamental aspects and recent advances in transition metal nitrides as electrocatalysts for hydrogen evolution reaction: A review. *Curr. Opin. Solid State Mater. Sci.* **2020**, *24*, 100805. [[CrossRef](#)]
86. Jaramillo, T.F.; Jørgensen, K.P.; Bonde, J.; Nielsen, J.H.; Horch, S.; Chorkendorff. Identification of Active Edge Sites for Electrochemical H₂ Evolution from MoS₂ Nanocatalysts. *Science* **2007**, *317*, 100–102. [[CrossRef](#)]
87. Hua, W.; Sun, H.; Xu, F.; Wang, J. A review and perspective on molybdenum-based electrocatalysts for hydrogen evolution reaction. *Rare Met.* **2020**, *39*, 335–351. [[CrossRef](#)]
88. BROWN, D.E.; MAHMOOD, M.N.; MAN, M.C.M.; TURNER, A.K. Preparation and Characterization of Low Overvoltage Transition Metal Alloy Electrocatalysts for Hydrogen Evolution in Alkaline Solutions. *Electrochim. Acta* **1984**, *29*, 1551–1556. [[CrossRef](#)]
89. Nairan, A.; Zou, P.; Liang, C.; Liu, J.; Wu, D.; Liu, P.; Yang, C. NiMo Solid Solution Nanowire Array Electrodes for Highly Efficient Hydrogen Evolution Reaction. *Adv. Funct. Mater.* **2019**, *29*, 1903747. [[CrossRef](#)]
90. Yu, Z.Y.; Duan, Y.; Gao, M.R.; Lang, C.C.; Zheng, Y.R.; Yu, S.H. A one-dimensional porous carbon-supported Ni/Mo₂C dual catalyst for efficient water splitting. *Chem. Sci.* **2017**, *8*, 968–973. [[CrossRef](#)]
91. Zhang, X.; Su, H.; Du, X. A nickel molybdenum oxide nanoarray as an efficient and stable electrocatalyst for overall water splitting. *New J. Chem.* **2020**, *44*, 8176–8182. [[CrossRef](#)]
92. Yu, Z.; Lang, C.; Gao, M.; Chen, Y.; Fu, Q.; Duan, Y.; Yu, S. Ni–Mo–O nanorod-derived composite catalysts for efficient alkaline water-to-hydrogen conversion via urea electrolysis. *Energy Environ. Sci.* **2018**, *11*, 1890–1897. [[CrossRef](#)]
93. Xu, B.; Sun, Y.; Chen, Z.; Zhao, S.; Yang, X.; Zhang, H.; Li, C. Facile and large-scale preparation of Co/Ni-MoO₂ composite as high-performance electrocatalyst for hydrogen evolution reaction. *Int. J. Hydrogen Energy* **2018**, *43*, 20721–20726. [[CrossRef](#)]
94. Hinnemann, B.; Moses, P.G.; Bonde, J.; Jørgensen, K.P.; Nielsen, J.H.; Horch, S.; Chorkendorff; Nørskov, J.K. Biomimetic Hydrogen Evolution: MoS₂ Nanoparticles as Catalyst for Hydrogen Evolution. *J. Am. Chem. Soc.* **2005**, *127*, 5308–5309. [[CrossRef](#)]
95. Vairy, D.; Salehi, M.; Silva, R.; Fujita, T.; Chen, M.; Asefa, T.; Shenoy, V.B.; Eda, G.; Chhowalla, M. Conducting MoS₂ nanosheets as catalysts for hydrogen evolution reaction. *Nano Lett.* **2013**, *13*, 6222–6227. [[CrossRef](#)]
96. Dai, X.; Du, K.; Li, Z.; Liu, M.; Ma, Y.; Sun, H.; Zhang, X.; Yang, Y. Co-Doped MoS₂ Nanosheets with the Dominant CoMoS Phase Coated on Carbon as an Excellent Electrocatalyst for Hydrogen Evolution. *ACS Appl. Mater. Interfaces* **2015**, *7*, 27242–27253. [[CrossRef](#)]
97. Wu, Z.; Guo, J.; Wang, J.; Liu, R.; Xiao, W.; Xuan, C.; Xia, K.; Wang, D. Hierarchically Porous Electrocatalyst with Vertically Aligned Defect-Rich CoMoS Nanosheets for the Hydrogen Evolution Reaction in an Alkaline Medium. *ACS Appl. Mater. Interfaces* **2017**, *9*, 5288–5294. [[CrossRef](#)]

98. Xu, S.; Li, D.; Wu, P. One-Pot, Facile, and Versatile Synthesis of Monolayer MoS₂/WS₂ Quantum Dots as Bioimaging Probes and Efficient Electrocatalysts for Hydrogen Evolution Reaction. *Adv. Funct. Mater.* **2015**, *25*, 1127–1136. [[CrossRef](#)]
99. Zheng, F.; Huang, N.; Peng, R.; Ding, Y.; Li, G.; Xia, Z.; Sun, P.; Sun, X.; Geng, J. Cobalt-doped molybdenum disulfide in-situ grown on graphite paper with excellent electrocatalytic activity for triiodide evolution. *Electrochim. Acta* **2018**, *263*, 328–337. [[CrossRef](#)]
100. Li, Y.; Zhang, H.; Jiang, M.; Kuang, Y.; Wang, H.; Sun, X. Amorphous Co–Mo–S ultrathin films with low-temperature sulfurization as high-performance electrocatalysts for the hydrogen evolution reaction. *J. Mater. Chem. A* **2016**, *4*, 13731–13735. [[CrossRef](#)]
101. Kwon, I.S.; Kwak, I.H.; Debela, T.T.; Abbas, H.G.; Park, Y.C.; Ahn, J.P.; Park, J.; Kang, H.S. Se-Rich MoSe₂ Nanosheets and Their Superior Electrocatalytic Performance for Hydrogen Evolution Reaction. *ACS Nano* **2020**, *14*, 6295–6304. [[CrossRef](#)] [[PubMed](#)]
102. Luo, Z.; Ouyang, Y.; Zhang, H.; Xiao, M.; Ge, J.; Jiang, Z.; Wang, J.; Tang, D.; Cao, X.; Liu, C.; et al. Chemically activating MoS₂ via spontaneous atomic palladium interfacial doping towards efficient hydrogen evolution. *Nat. Commun.* **2018**, *3*, 2120. [[CrossRef](#)] [[PubMed](#)]
103. Li, L.; Qin, Z.; Ries, L.; Hong, S.; Michel, T.; Yang, J.; Salameh, C.; Bechelany, M.; Miele, P.; Kaplan, D.; et al. Role of Sulfur Vacancies and Undercoordinated Mo Regions in MoS₂ Nanosheets toward the Evolution of Hydrogen. *ACS Nano* **2019**, *13*, 6824–6834. [[CrossRef](#)] [[PubMed](#)]
104. Li, G.; Fu, C.; Wu, J.; Rao, J.; Liou, S.-C.; Xu, X.; Shao, B.; Liu, K.; Liu, E.; Kumar, N.; et al. Synergistically creating sulfur vacancies in semimetal-supported amorphous MoS₂ for efficient hydrogen evolution. *Appl. Catal. B Environ.* **2019**, *254*, 1–6. [[CrossRef](#)]
105. Li, X.; Yu, J.; Jia, J.; Wang, A.; Zhao, L.; Xiong, T.; Liu, H.; Zhou, W. Confined distribution of platinum clusters on MoO₂ hexagonal nanosheets with oxygen vacancies as a high-efficiency electrocatalyst for hydrogen evolution reaction. *Nano Energy* **2019**, *62*, 127–135. [[CrossRef](#)]
106. Liu, S.; Chen, C.; Zhang, Y.; Zheng, Q.; Zhang, S.; Mu, X.; Chen, C.; Ma, J.; Mu, S. Vacancy-coordinated hydrogen evolution reaction on MoO_{3-x} anchored atomically dispersed MoRu pairs. *J. Mater. Chem. A* **2019**, *7*, 14466–14472. [[CrossRef](#)]
107. Wijten, J.H.J.; Riemersma, R.L.; Gauthier, J.; Mandemaker, L.D.B.; Verhoeven, M.; Hofmann, J.P.; Chan, K.; Weckhuysen, B.M. Electrolyte Effects on the Stability of Ni–Mo Cathodes for the Hydrogen Evolution Reaction. *ChemSusChem* **2019**, *12*, 3491–3500. [[CrossRef](#)]
108. Kagkoura, A.; Canton Vitoria, R.; Vallan, L.; Hernandez Ferrer, J.; Benito, A.M.; Maser, W.K.; Arenal, R.; Tagmatarchis, N. Bottom-Up Synthesized MoS₂ Interfacing Polymer Carbon Nanodots with Electrocatalytic Activity for Hydrogen Evolution. *Chem. Eur. J.* **2020**, *26*, 6635–6642. [[CrossRef](#)]
109. Xiao, Z.; Xie, C.; Wang, Y.; Chen, R.; Wang, S. Recent advances in defect electrocatalysts: Preparation and characterization. *J. Energy Chem.* **2021**, *53*, 208–225. [[CrossRef](#)]
110. Li, B.L.; Zou, H.L.; Tian, J.K.; Chen, G.; Wang, X.H.; Duan, H.; Li, X.L.; Shi, Y.; Chen, J.R.; Li, L.J.; et al. Principle of proximity: Plasmonic hot electrons motivate donator-adjacent semiconductor defects with enhanced electrocatalytic hydrogen evolution. *Nano Energy* **2019**, *60*, 689–700. [[CrossRef](#)]
111. Li, J.; Hong, W.; Jian, C.; Cai, Q.; He, X.; Liu, W. High-performance hydrogen evolution at a MoSe₂–Mo₂C seamless heterojunction enabled by efficient charge transfer. *J. Mater. Chem. A* **2020**, *8*, 6692–6698. [[CrossRef](#)]
112. Yin, Z.; Sun, Y.; Jiang, Y.; Yan, F.; Zhu, C.; Chen, Y. Hierarchical Cobalt-Doped Molybdenum-Nickel Nitride Nanowires as Multifunctional Electrocatalysts. *ACS Appl. Mater. Interfaces* **2019**, *11*, 27751–27759. [[CrossRef](#)] [[PubMed](#)]
113. Rodene, D.D.; Eladgham, E.H.; Gupta, R.B.; Arachchige, I.U.; Tallapally, V. Crystal Structure and Composition-Dependent Electrocatalytic Activity of Ni–Mo Nanoalloys for Water Splitting To Produce Hydrogen. *ACS Appl. Energy Mater.* **2019**, *2*, 7112–7120. [[CrossRef](#)]
114. Gong, Q.; Cheng, L.; Liu, C.; Zhang, M.; Feng, Q.; Ye, H.; Zeng, M.; Xie, L.; Liu, Z.; Li, Y. Ultrathin MoS_{2(1-x)}Se_{2x} Alloy Nanoflakes for Electrocatalytic Hydrogen Evolution Reaction. *ACS Catal.* **2015**, *5*, 2213–2219. [[CrossRef](#)]
115. Lu, C.; Tranca, D.; Zhang, J.; Rodri Guez Hernandez, F.N.; Su, Y.; Zhuang, X.; Zhang, F.; Seifert, G.; Feng, X. Molybdenum Carbide-Embedded Nitrogen-Doped Porous Carbon Nanosheets as Electrocatalysts for Water Splitting in Alkaline Media. *ACS Nano* **2017**, *11*, 3933–3942. [[CrossRef](#)]

116. Ge, X.; Chen, L.; Zhang, L.; Wen, Y.; Hirata, A.; Chen, M. Nanoporous metal enhanced catalytic activities of amorphous molybdenum sulfide for high-efficiency hydrogen production. *Adv. Mater.* **2014**, *26*, 3100–3104. [[CrossRef](#)]
117. Tan, Y.; Liu, P.; Chen, L.; Cong, W.; Ito, Y.; Han, J.; Guo, X.; Tang, Z.; Fujita, T.; Hirata, A.; et al. Monolayer MoS₂ films supported by 3D nanoporous metals for high-efficiency electrocatalytic hydrogen production. *Adv. Mater.* **2014**, *26*, 8023–8028. [[CrossRef](#)]
118. Kumar, R.; Ahmed, Z.; Kaur, H.; Bera, C.; Bagchi, V. Probing into the effect of heterojunctions between Cu/Mo₂C/Mo₂N on HER performance. *Catal. Sci. Technol.* **2020**, *10*, 2213–2220. [[CrossRef](#)]
119. Toghraei, A.; Shahrabi, T.; Barati Darband, G. Electrodeposition of self-supported Ni-Mo-P film on Ni foam as an affordable and high-performance electrocatalyst toward hydrogen evolution reaction. *Electrochim. Acta* **2020**, *335*, 135643. [[CrossRef](#)]
120. Xie, J.; Xin, J.; Cui, G.; Zhang, X.; Zhou, L.; Wang, Y.; Liu, W.; Wang, C.; Ning, M.; Xia, X.; et al. Vertically aligned oxygen-doped molybdenum disulfide nanosheets grown on carbon cloth realizing robust hydrogen evolution reaction. *Inorg. Chem. Front.* **2016**, *3*, 1160–1166. [[CrossRef](#)]
121. Xie, S.; Sun, B.; Sun, H.; Zhan, K.; Zhao, B.; Yan, Y.; Xia, B.Y. Engineering of molybdenum sulfide nanostructures towards efficient electrocatalytic hydrogen evolution. *Int. J. Hydrogen Energy* **2019**, *44*, 15009–15016. [[CrossRef](#)]
122. Xie, J.; Zhang, J.; Li, S.; Grote, F.; Zhang, X.; Zhang, H.; Wang, R.; Lei, Y.; Pan, B.; Xie, Y. Controllable disorder engineering in oxygen-incorporated MoS₂ ultrathin nanosheets for efficient hydrogen evolution. *J. Am. Chem. Soc.* **2013**, *135*, 17881–17888. [[CrossRef](#)] [[PubMed](#)]
123. Hu, C.; Jiang, Z.; Zhou, W.; Guo, M.; Yu, T.; Luo, X.; Yuan, C. Wafer-Scale Sulfur Vacancy-Rich Monolayer MoS₂ for Massive Hydrogen Production. *J. Phys. Chem. Lett.* **2019**, *10*, 4763–4768. [[CrossRef](#)] [[PubMed](#)]
124. Xu, C.; Peng, S.; Tan, C.; Ang, H.; Tan, H.; Zhang, H.; Yan, Q. Ultrathin S-doped MoSe₂ nanosheets for efficient hydrogen evolution. *J. Mater. Chem. A* **2014**, *2*, 5597–5601. [[CrossRef](#)]
125. Guo, Y.; Zhang, X.; Zhang, X.; You, T. Defect- and S-rich ultrathin MoS₂ nanosheet embedded N-doped carbon nanofibers for efficient hydrogen evolution. *J. Mater. Chem. A* **2015**, *3*, 15927–15934. [[CrossRef](#)]
126. Huang, H.; Chen, L.; Liu, C.; Liu, X.; Fang, S.; Liu, W.; Liu, Y. Hierarchically nanostructured MoS₂ with rich in-plane edges as a high-performance electrocatalyst for the hydrogen evolution reaction. *J. Mater. Chem. A* **2016**, *4*, 14577–14585. [[CrossRef](#)]
127. Yin, Z.; Sun, Y.; Zhu, C.; Li, C.; Zhang, X.; Chen, Y. Bimetallic Ni–Mo nitride nanotubes as highly active and stable bifunctional electrocatalysts for full water splitting. *J. Mater. Chem. A* **2017**, *5*, 13648–13658. [[CrossRef](#)]
128. Yang, Q.; He, Y.; Fan, Y.; Li, F.; Chen, X. Exfoliation of the defect-rich MoS₂ nanosheets to obtain nanodots modified MoS₂ thin nanosheets for electrocatalytic hydrogen evolution. *J. Mater. Sci. Mater. Electron.* **2017**, *28*, 7413–7418. [[CrossRef](#)]
129. Hou, Y.; Pang, H.; Zhang, L.; Li, B.; Xin, J.; Li, K.; Ma, H.; Wang, X.; Tan, L. Highly dispersive bimetallic sulfides afforded by crystalline polyoxometalate-based coordination polymer precursors for efficient hydrogen evolution reaction. *J. Power Sources* **2020**, *446*, 227319. [[CrossRef](#)]
130. Xiao, W.; Zhang, L.; Bukhvalov, D.; Chen, Z.; Zou, Z.; Shang, L.; Yang, X.; Yan, D.; Han, F.; Zhang, T. Hierarchical ultrathin carbon encapsulating transition metal doped MoP electrocatalysts for efficient and pH-universal hydrogen evolution reaction. *Nano Energy* **2020**, *70*, 104445. [[CrossRef](#)]
131. Kiriya, D.; Lobaccaro, P.; Nyein, H.Y.; Taheri, P.; Hettick, M.; Shiraki, H.; Sutter-Fella, C.M.; Zhao, P.; Gao, W.; Maboudian, R.; et al. General Thermal Texturization Process of MoS₂ for Efficient Electrocatalytic Hydrogen Evolution Reaction. *Nano Lett.* **2016**, *16*, 4047–4053. [[CrossRef](#)] [[PubMed](#)]
132. Sun, K.; Liu, Y.; Pan, Y.; Zhu, H.; Zhao, J.; Zeng, L.; Liu, Z.; Liu, C. Targeted bottom-up synthesis of 1T-phase MoS₂ arrays with high electrocatalytic hydrogen evolution activity by simultaneous structure and morphology engineering. *Nano Res.* **2018**, *11*, 4368–4379. [[CrossRef](#)]
133. Nolan, H.; McEvoy, N.; O'Brien, M.; Berner, N.C.; Yim, C.; Hallam, T.; McDonald, A.R.; Duesberg, G.S. Molybdenum disulfide/pyrolytic carbon hybrid electrodes for scalable hydrogen evolution. *Nanoscale* **2014**, *6*, 8185–8191. [[CrossRef](#)] [[PubMed](#)]
134. Sun, X.; Dai, J.; Guo, Y.; Wu, C.; Hu, F.; Zhao, J.; Zeng, X.; Xie, Y. Semimetallic molybdenum disulfide ultrathin nanosheets as an efficient electrocatalyst for hydrogen evolution. *Nanoscale* **2014**, *6*, 8359–8367. [[CrossRef](#)] [[PubMed](#)]

135. Deng, J.; Yuan, W.; Ren, P.; Wang, Y.; Deng, D.; Zhang, Z.; Bao, X. High-performance hydrogen evolution electrocatalysis by layer-controlled MoS₂ nanosheets. *RSC Adv.* **2014**, *4*, 34733–34738. [[CrossRef](#)]
136. Muralikrishna, S.; Manjunath, K.; Samrat, D.; Reddy, V.; Ramakrishnappa, T.; Nagaraju, D.H. Hydrothermal synthesis of 2D MoS₂ nanosheets for electrocatalytic hydrogen evolution reaction. *RSC Adv.* **2015**, *5*, 89389–89396. [[CrossRef](#)]
137. Gao, X.; Qi, J.; Wan, S.; Zhang, W.; Wang, Q.; Cao, R. Conductive Molybdenum Sulfide for Efficient Electrocatalytic Hydrogen Evolution. *Small* **2018**, *14*, 1803361. [[CrossRef](#)] [[PubMed](#)]
138. Cao, B.; Neuefeind, J.C.; Adzic, R.R.; Khalifah, P.G. Molybdenum nitrides as oxygen reduction reaction catalysts: Structural and electrochemical studies. *Inorg. Chem.* **2015**, *54*, 2128–2136. [[CrossRef](#)]
139. Cao, B.; Veith, G.M.; Diaz, R.E.; Liu, J.; Stach, E.A.; Adzic, R.R.; Khalifah, P.G. Cobalt molybdenum oxynitrides: Synthesis, structural characterization, and catalytic activity for the oxygen reduction reaction. *Angew. Chem. Int. Ed.* **2013**, *52*, 10753–10757. [[CrossRef](#)]
140. Yin, J.; Yu, Z.; Gao, F.; Wang, J.; Pang, H.; Lu, Q. Low-symmetry iron oxide nanocrystals bound by high-index facets. *Angew. Chem. Int. Ed.* **2010**, *49*, 6328–6332. [[CrossRef](#)]
141. Zhang, C.; Zou, X.; Du, Z.; Gu, J.; Li, S.; Li, B.; Yang, S. Atomic Layers of MoO₂ with Exposed High-Energy (010) Facets for Efficient Oxygen Reduction. *Small* **2018**, *14*, 1703960. [[CrossRef](#)] [[PubMed](#)]
142. Lin, L.; Yang, Z.; Jiang, Y.; Xu, A. Nonprecious Bimetallic (Fe,Mo)–N/C Catalyst for Efficient Oxygen Reduction Reaction. *ACS Catal.* **2016**, *6*, 4449–4454. [[CrossRef](#)]
143. Yasin, A.S.; Liu, B.; Wu, N.; Musho, T. Density functional theory evaluation of cation-doped bismuth molybdenum oxide photocatalysts for nitrogen fixation. *Comp. Mater. Sci.* **2019**, *158*, 65–75. [[CrossRef](#)]
144. Li, Q.; Qiu, S.; Liu, C.; Liu, M.; He, L.; Zhang, X.; Sun, C. Computational Design of Single-Molybdenum Catalysts for the Nitrogen Reduction Reaction. *J. Phys. Chem. C* **2019**, *123*, 2347–2352. [[CrossRef](#)]
145. Zhao, J.; Cui, C.; Wang, H.; Han, J.; Zhu, X.; Ge, Q. Insights into the Mechanism of Ammonia Decomposition on Molybdenum Nitrides Based on DFT Studies. *J. Phys. Chem. C* **2018**, *123*, 554–564. [[CrossRef](#)]
146. Zhao, X.; Zhang, X.; Xue, Z.; Chen, W.; Zhou, Z.; Mu, T. Fe nanodot-decorated MoS₂ nanosheets on carbon cloth: An efficient and flexible electrode for ambient ammonia synthesis. *J. Mater. Chem. A* **2019**, *7*, 27417–27422. [[CrossRef](#)]
147. Zeng, L.; Li, X.; Chen, S.; Wen, J.; Rahmati, F.; van der Zalm, J.; Chen, A. Highly boosted gas diffusion for enhanced electrocatalytic reduction of N₂ to NH₃ on 3D hollow Co-MoS₂ nanostructures. *Nanoscale* **2020**, *12*, 6029–6036. [[CrossRef](#)]
148. Zhang, G.; Ji, Q.; Zhang, K.; Chen, Y.; Li, Z.; Liu, H.; Li, J.; Qu, J. Triggering surface oxygen vacancies on atomic layered molybdenum dioxide for a low energy consumption path toward nitrogen fixation. *Nano Energy* **2019**, *59*, 10–16. [[CrossRef](#)]
149. Zeng, L.; Chen, S.; van der Zalm, J.; Li, X.; Chen, A. Sulfur vacancy-rich N-doped MoS₂ nanoflowers for highly boosting electrocatalytic N₂ fixation to NH₃ under ambient conditions. *Chem. Commun.* **2019**, *55*, 7386–7389. [[CrossRef](#)]
150. Li, Y.; Wang, C.; Cui, M.; Chen, S.; Ma, T. A novel strategy to synthesize CoMoO₄ nanotube as highly efficient oxygen evolution reaction electrocatalyst. *Catal. Commun.* **2019**, *131*, 105800. [[CrossRef](#)]
151. Zhao, X.; Meng, J.; Yan, Z.; Cheng, F.; Chen, J. Nanostructured NiMoO₄ as active electrocatalyst for oxygen evolution. *Chin. Chem. Lett.* **2019**, *30*, 319–323. [[CrossRef](#)]
152. Zhang, J.; Wang, T.; Pohl, D.; Rellinghaus, B.; Dong, R.; Liu, S.; Zhuang, X.; Feng, X. Interface Engineering of MoS₂/Ni₃S₂ Heterostructures for Highly Enhanced Electrochemical Overall-Water-Splitting Activity. *Angew. Chem. Int. Ed.* **2016**, *55*, 6702–6707. [[CrossRef](#)] [[PubMed](#)]
153. Guo, C.; Sun, X.; Kuang, X.; Gao, L.; Zhao, M.; Qu, L.; Zhang, Y.; Wu, D.; Ren, X.; Wei, Q. Amorphous Co-doped MoO_x nanospheres with a core-shell structure toward an effective oxygen evolution reaction. *J. Mater. Chem. A* **2019**, *7*, 1005–1012. [[CrossRef](#)]
154. Hao, L.; Yu, J.; Xu, X.; Yang, L.; Xing, Z.; Dai, Y.; Sun, Y.; Zou, J. Nitrogen-doped MoS₂/carbon as highly oxygen-permeable and stable catalysts for oxygen reduction reaction in microbial fuel cells. *J. Power Sources* **2017**, *339*, 68–79. [[CrossRef](#)]
155. Sun, T.; Wu, Q.; Che, R.; Bu, Y.; Jiang, Y.; Li, Y.; Yang, L.; Wang, X.; Hu, Z. Alloyed Co–Mo Nitride as High-Performance Electrocatalyst for Oxygen Reduction in Acidic Medium. *ACS Catal.* **2015**, *5*, 1857–1862. [[CrossRef](#)]

156. Yang, L.; Yu, J.; Wei, Z.; Li, G.; Cao, L.; Zhou, W.; Chen, S. Co-N-doped MoO₂ nanowires as efficient electrocatalysts for the oxygen reduction reaction and hydrogen evolution reaction. *Nano Energy* **2017**, *41*, 772–779. [[CrossRef](#)]
157. Chen, S.; Jang, H.; Wang, J.; Qin, Q.; Liu, X.; Cho, J. Bimetallic metal–organic framework-derived MoFe-PC microspheres for electrocatalytic ammonia synthesis under ambient conditions. *J. Mater. Chem. A* **2020**, *8*, 2099–2104. [[CrossRef](#)]
158. Yang, D.; Chen, T.; Wang, Z. Electrochemical reduction of aqueous nitrogen (N₂) at a low overpotential on (110)-oriented Mo nanofilm. *J. Mater. Chem. A* **2017**, *5*, 18967–18971. [[CrossRef](#)]
159. Chu, K.; Liu, Y.; Li, Y.; Guo, Y.; Tian, Y.; Zhang, H. Multi-functional Mo-doping in MnO₂ nanoflowers toward efficient and robust electrocatalytic nitrogen fixation. *Appl. Catal. B Environ.* **2020**, *264*, 118525. [[CrossRef](#)]

Publisher's Note: MDPI stays neutral with regard to jurisdictional claims in published maps and institutional affiliations.



© 2020 by the authors. Licensee MDPI, Basel, Switzerland. This article is an open access article distributed under the terms and conditions of the Creative Commons Attribution (CC BY) license (<http://creativecommons.org/licenses/by/4.0/>).